TECHNISCHE UNIVERSITÄT WIEN
Vienna University of Technology

MASTER THESIS

Structural and Mechanical Properties of Collagen During Embryonic Development

Submitted in partial fulfilment of the requirements for the academic degree of Master of Science, under supervision of

Dr. Orestis ANDRIOTIS

Univ. Prof. Dipl.-Ing. Dr.sc.nat. Philipp J. THURNER

at

Institute of Lightweight Design and Structural Biomechanics - E317

Vienna University of Technology

by

Nina Sophia Hennicke

Matric.no. 1528640

Vienna, March 2018

Affidavit

I declare in lieu of oath, that I wrote this thesis and performed the associated research myself, using only literature cited in this volume. If text passages from sources are used literally, they are marked as such.

I confirm that this work is original and has not been submitted elsewhere for any examination, nor is it currently under consideration for a thesis elsewhere.

Vienna, March 2018

Signature

Abstract

The mechanical properties of collagen fibrils in tendon tissue have been a focus of scientific interest as their function to transfer loads from muscle to bone are a critical aspect of locomotion. However, efforts to heal and regenerate tendon are still challenged by the limited knowledge on its natural development within the body. Especially the effects of intrafibrillar interactions on the mechanical properties of individual collagen fibrils is not yet fully understood. The functional characterisation of individual collagen fibrils during embryonic development can provide new perspectives on collagen structure, mechanics and maturation. Understanding the assembly and mechanics of individual early collagen fibrils has major implications for tissue morphogenesis and repair. The goal of this thesis was to investigate changes in mechanical properties of individual tendon collagen fibrils during embryonic chick development. In this context enzymatic cross-linking is one point of focus as the chemical modification in similar chicks is known as it has been studied before. Nanomechanical assessment of individual collagen fibrils was conducted in phosphate buffered saline through cantilever-based nanoindentation via atomic force microscopy which proved to be a promising tool for research on tissue biomechanics. With this technique collagen fibrils of less than 30 nm during embryonic development in chicks from stage HH37 to HH41 were mechanically characterised. The recorded data was analysed with the Oliver-Pharr method to calculate the indentation moduli of individual collagen fibrils at the mentioned developmental stages. The experiments showed that the indentation moduli of single collagen fibrils during embryonic chick development increase non-linearly from 1.63 MPa to 2.74 MPa from development stage HH38 to HH41, respectively ($p < 0.05$). This indicates an accumulation of cross-links during continued embryonic development. Also, small but significant changes in fibril diameter after HH39 could be determined ($p < 0.05$). Furthermore, the effect of enzymatic cross-linking on the indentation modulus of collagen fibrils harvested from chick embryos that had been treated *in ovo* with β-aminopropionitrile to inhibit lysyl-oxidase-mediated cross-linking were investigated. The treated collagen fibrils showed a significantly lower indentation modulus than fibrils treated with saline in a comparison group ($p < 0.05$). This suggests that lysyl-oxidase-mediated cross-linking is partly, if not completely, responsible for the non-linearly increasing indentation modulus of collagen fibrils during embryonic development and therefore contributes to changes in mechanical properties of tendon during development.

Acknowledgments

I am very grateful to all the people who helped and advised me throughout this thesis. My deepest gratitude goes to my family who always encouraged and supported me during my studies.

I would especially like to thank Professor Philipp Thurner for supervising this thesis. I am also very thankful to Dr. Orestis Andriotis who assisted in supervising me and whose support has been of great value.

Content

Nomenclature

AFM	atomic force microscope
AGE	advanced glycation end product
BAPN	β-aminopropionitrile
DNA	deoxyribonucleic acid
ECM	extracellular matrix
ER	endoplasmic reticulum
FV-AFM	force volume atomic force microscopy
GAG	glycosaminoglycan
Gly	glycine
HH	Hamburger-Hamilton
Hyp	hydroxyproline
IQR	interquartile range
LOX	lysyl oxidase
mRNA	messenger ribonucleic acid
OM	optical microscope
PBS	phosphate buffered saline
PID	proportional-integral-differential
PPI	peptidyl-prolyl cis-trans-isomerase
QI™	quantitative imaging
ROI	region of interest
SD	standard deviation
SFM	Scanning Force Microscope
SPM	Scanning Probe Microscope

1 Introduction

1.1 Background

The mechanical stability and function of vertebrae and some invertebrates is enabled by connective tissues that carry tensile and compressive loads. A main component of most load bearing connective tissues are collagenous proteins. In the human body collagens make up approx. 25-35% of the overall protein content. Collagens are responsible for maintaining structural integrity and mechanical function of tissues. This makes collagens one of the most important proteins in the body from a biomechanical point of view. They occur in especially high concentrations in musculoskeletal load-bearing tissues like bone, tendon, ligament, skin and cartilage. Collagen molecules, also called tropo-collagen molecules, consist of three left-handed coiled polypeptide chains. More than 28 different types of collagens have been identified. Type I tropo-collagen molecules consist of two α1-chains and one α2-chain. This type is the most abundant of collagen and its molecules assemble into larger, fibrillar structures. These collagen fibrils are mainly made up of tropocollagen molecules that are twisted together in a rope like configuration with a nanoscale diameter. While highest in type I collagen content, they are generally amalgamations of different types of collagen molecules, which interact. Collagen fibrils provide a structural basis to resist tensile, shear and compressive forces. They build up progressively into larger structures on the macroscale. This hierarchical architecture of connective tissues is also fundamentally responsible for their mechanical properties. Furthermore, the mechanical properties of connective tissues are particularly depending on the nanostructure of the collagen fibrils contained within them and molecular interactions within or between these fibrils. Small changes at the nanoscale are thought to affect the macroscale structure of the tissue and through a “butterfly” effect can result in significant mechanical alterations. The relation between structure and mechanical function is also of high importance from a biomimetic point of view, i.e. for the design of artificial materials or systems with similar property propagation. For these reasons, mechanical assessment at the nanoscale can contribute to the understanding of structure-function relationships of tissues. Local force probe techniques, e.g. atomic force microscopy, allow localized mechanical measurements on the nanometre scale which makes direct testing of individual collagen fibrils possible. Atomic force microscopy (AFM) was firstly used to image single collagen fibrils by Chernoff et. al. in 1992 [1]. Since then, AFM has become a popular technique not only to image but also mechanically assess collagen at the individual fibril level. Additionally, a number of AFM techniques to perform

indentation measurements on small structures and fragile materials have evolved so that local variations at micro- and nanoscale level can be detected.

Although there has been data recorded on embryonic chick tendon with regards to proteomics and the evolution of covalent cross-links, knowledge on the effect of these cross-links on collagen tissue mechanics is scarce. Evolving cross-links during growth and development of collagenous tissues are thought to alter the mechanical properties of these tissues. However, the effect of cross-links on tendon at the level of individual collagen fibrils remains unclear. A few recent studies on embryonic collagen development demonstrated that mechanical properties are not consistently correlated with matrix content and organization [2]–[6]. Characterisation of mechanical properties is often foregone in favour of information on tissue morphology and biochemical content to assess functional tissue formation. However, lack of consistent correlation of matrix morphology and content with mechanical property changes during embryonic development of tendon indicates a need to characterise functional properties of newly forming collagen rich tissues. In chick embryos cross-linking density was found to vary as a function of developmental stage from measurements with tandem mass spectrometry [7]. Understanding the influence of cross-links on the structural and mechanical properties of individual collagen fibrils during embryonic development is an important factor for the characterisation of natural tissue assembly in tendon. Presently, aberrant mechanical properties of scarred, tendon tissues are associated with abnormal matrix content and organization. Therefore, most strategies to improve healing and regeneration of tendon have primarily focused on protein expression and tissue microstructure. Functional characterisation of evolving cross-links in embryonic tendon may improve clinical treatment approaches for regenerating, repairing or replacing injured tendon since it is a common site of sports or work-related injury with poor innate healing ability.

1.2 Objective

Tendon is a connective tissue that is mainly composed of collagen type I and therefore is a preferred organic sample tissue for collagen studies. It is formed in the early stages of fetal development and tissue samples can be easily extracted from chick embryos. At the beginning of gestation embryonic tendon is highly cellular and exhibits a sparse disorganised collagen fibre matrix. There is little information on the factors affecting mechanical properties of tendon during the early developmental stages. However, the mature tendon is composed of highly aligned and cross-linked collagen fibrils which provide sufficient stiffness and tensile strength

for effective functionality. The aim of this thesis is to investigate structural and mechanical properties of developing collagen fibrils and, via additional data available through a collaborator, to show how enzymatic cross-linking contributes in their mechanical properties. The AFM allows direct local evaluation of mechanical properties and structure on the nanometre scale. With AFM, topographic measurements and force-indentation data can simultaneously be collected through a force-volume topographic map. Both imaging and nanoindentation experiments were performed on embryonic chick collagen fibrils using AFM, to provide information about the regional variations in tissue structure and elastic modulus.

1.3 Structure of Thesis

This thesis is sectioned into seven chapters. Chapter 2 gives an introduction to the topic of collagen. In further detail, collagen synthesis in the human body and assembly into hierarchical structures in tendon are described. The chapter also gives a short overview on concepts of cross-linking between collagen molecules, mechanical properties of single collagen fibrils and a summary on collagen formation during embryonic chick development.

Chapter 3 is dedicated to the working principles of atomic force microscopy, its components and basic imaging modes.

Chapter 4 describes the materials and methods used for the experiments of this thesis. A focus is put on AFM imaging and cantilever based nanoindentation. But this chapter also includes sample preparation and analysis methods applied to the recorded data.

In Chapter 5 the analysed results gained from the nanoindentation experiments are presented and described.

Chapter 6 discusses the afore mentioned results and their statistical evaluation.

At last, chapter 7 concludes this thesis by giving a short summary on its investigations and findings as well as an outlook on prospective continuing experiments.

2 Collagen

As the most abundant protein in the body, collagen is, among other functions, essential as a structural component of the extracellular matrix (ECM) which endows tissues with their specific mechanical and biochemical properties. Collagen can be found in large quantities in various kinds of tissues like skin, bone, muscle, tendon, veins and teeth to name only a few. There are about 30 known types of collagens that differ in their amino acid composition, function and 3-dimensional conformation [8], [9].

2.1 Synthesis of Collagen Molecules

Like all proteins, the synthesis of collagen molecules starts with the transcription of DNA in the cell nucleus to mRNA. Depending on the type of collagen this mRNA strand can contain more than 50 exons. After splicing, capping and polyadenylation, the processed mRNA is translated by ribosomes at the rough ER into preprocollagen molecules which protrude into the lumen of the rough ER (see Figure 1). There, the molecules undergo multiple steps of post-translational modifications.

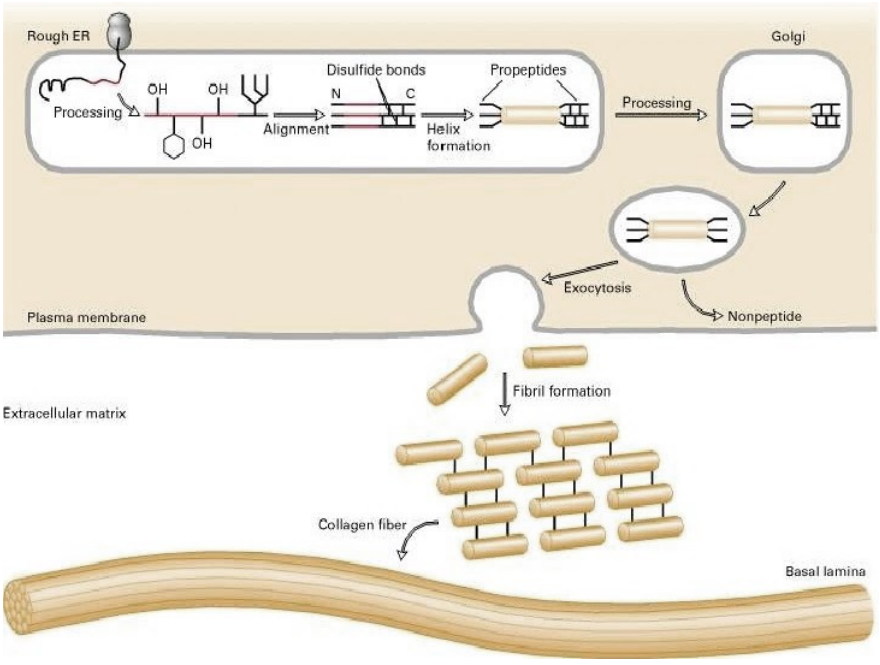

Figure 1: Synthesis of collagen fibril from mRNA translation to fibril formation [10]

For the fibril forming collagen type I, the modifications include primarily the hydroxylation of proline and lysine residues. The resulting 4-hydroxyproline is essential for the later formation

of intramolecular hydrogen bonds and thus thermal stability of the mature collagen. Whereas hydroxy lysine will form stable intermolecular cross-links between collagen fibrils and pose as an attachment site for carbohydrates.

After hydroxylation the globular structure of the C-propeptide is stabilized by intrachain disulphide bonds and a N-linked carbohydrate group is added to the peptide. The procollagen assembly into a triple helix begins with the alignment of the C-terminal domains of the three peptide chains. The efficient formation and folding of the chains depends highly on further enzymes (especially PPI) and chaperones (like HSP47). The fully formed triple helix is transported to the Golgi and packaged into secretory vesicles to be released into the extracellular space. There the C-propeptides and N-propeptides are cleaved off so that the fibril assembly can begin. [11], [12], [13]

2.2 Hierarchical Structure of Tendon

All proteins of the collagen family consist of a right-handed triple helix which is composed of three α-chains. Each chain forms a left-handed helix and supercoils around a central axis to form the triple helix [14]. To allow for a proper assembly of the three polypeptide chains, a hydrophobic peptide residue is present in every third position of each chain. Glycine, being the smallest amino acid, allows for the tightest packing during assembly. The peptide sequence therefore often follows the pattern Gly-X-Y in fibrous collagens. In that case, the small hydrophobic glycine residues are positioned in the centre of the triple helix and joined by hydrogen bonds while the other amino acids with more bulky side chains face the outside. This allows a close packaging along the central axis.

With 90% of the collagens found in animals and humans belonging to the fibril forming collagens (type I, II, III, V and XI), these are the most abundant types of collagen and the focus of this thesis. Fibril forming collagens have the ability to assemble into highly orientated supramolecular aggregates with a characteristic suprastructure. [11]

Within connective tissues, the molecules of collagen type I assemble parallel to each other into fibrils by axial staggering with a periodicity of 67 nm. They retain a distance of roughly 40 nm in axial direction between neighbouring molecules. This leads to a gap structure on this hierarchical level which in case of hard tissues like bone or tooth enamel would be used to store hydroxyapatite to form micro composites and improve load bearing properties. The ability for self-assembly of the molecules is encoded in their specific structure and involves hydrophobic

and electrostatic interactions. The fibrils are stabilized by covalent cross-links, which contribute to the mechanical resilience of the tissue as represented in Figure 2. [8], [9]

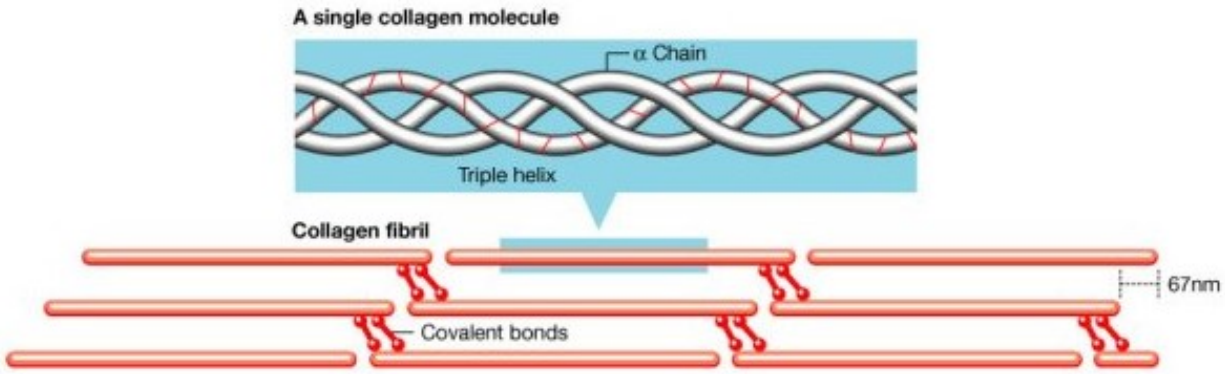

Figure 2: Staggering and covalent bonding of collagen molecules [15]

The resulting microfibrils further assemble into fibrils with a typical diameter of a few hundred nanometres. They are decorated with tightly bound proteoglycans which form a matrix between the fibrils. In the electron microscope and AFM, single fibrils are defined by their characteristic banding pattern with a periodicity of approx. 67 nm which is called D-period. This periodicity is based on a staggered arrangement of individual collagen monomers. The fibrils are then assembled into fascicles and finally into tendon as pictured in the overview in Figure 3. [9], [11], [16]

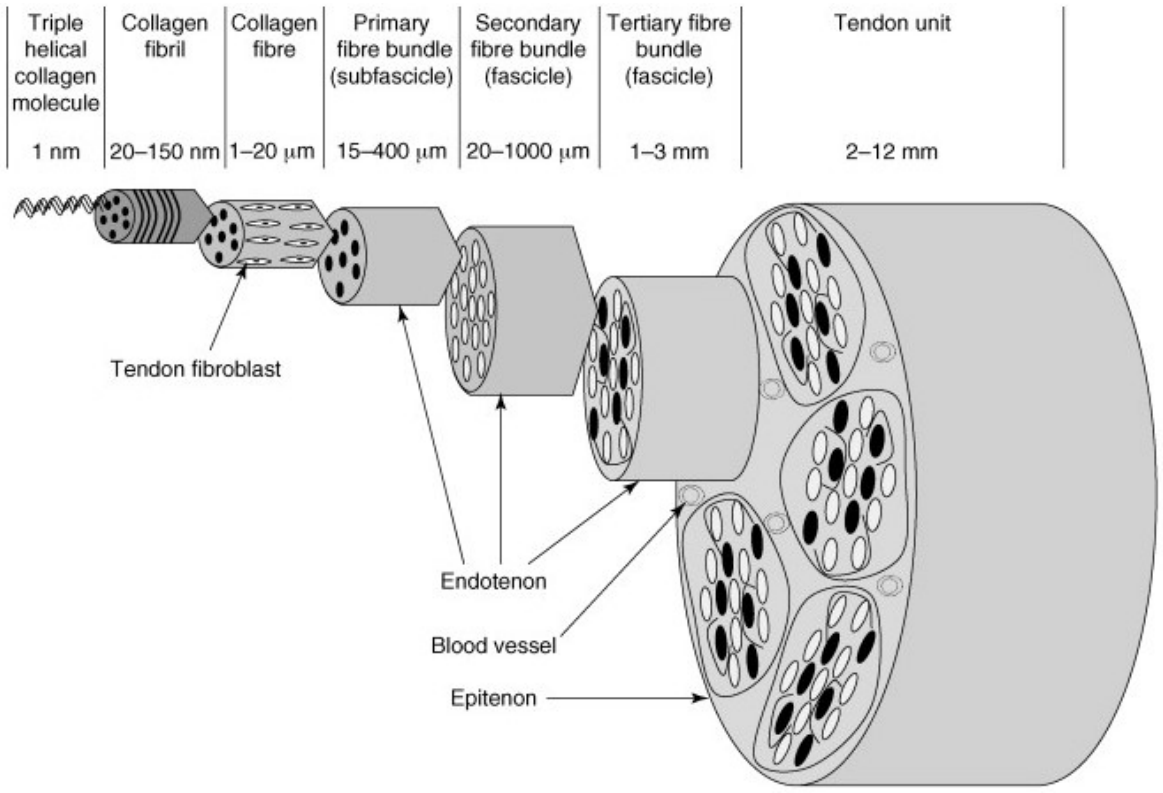

Figure 3: Overview on the hierarchical structure of tendon [17]

2.3 Collagen Cross-Linking

In previous studies cross-linking in collagen has been reported to increase mechanical properties of tendon tissue [18], [19]. However, these reports did not distinguish between intra- and interfibrillar cross-links as they were conducted on the fascicle scale level of tissue. Interfibrillar cross-links occur in high numbers between collagen fibrils and they are thought to be mainly responsible for the tangled spatial arrangement of collagen fibrils as well as the crimp surface structure of collagenous tissues [20]. These structural arrangements enhance mechanical properties of the tissue and oppose interfibrillar sliding. The formation of intrafibrillar cross-linking on the other hand is thought to significantly contribute to the mechanical strength and resilience of collagenous tissues at a lower level. In general, there are two main categories of collagen cross-links that differ in the formation origin of the cross-links.

2.3.1 Enzymatic Cross-Links

Enzymatic cross-links between collagen molecules are formed during fibril assembly in the tissue. Enzymes initiate oxidation and hydroxylation of specific residues located at the telopeptides. In collagen type I, lysine hydroxylation is induced by the enzyme lysyl oxidase (LOX) which catalyses the formation of aldehydes from lysine and hydroxy lysine residues. Spontaneous reactions of these aldehydes result in the formation of intermediate cross-links while the interaction of aldehydes with adjacent lysine residues forms aldimine cross-links. The presence of hydroxy lysine-derived telopeptide aldehydes also allows the formation of more stable ketoimine bonds. During maturation of the tissue the aldimine and ketoimine cross-links will later be converted by chemical reactions to histidine adducts and pyridinium cross-links respectively which are classified as non-reducible mature links. These mature trivalent cross-links also bridge a third collagen molecule. [6], [11], [21], [22]

2.3.2 Non-Enzymatic Cross-Links

Non-enzymatic cross-links occur at a later point in fibril formation than the enzyme induced cross-links and accumulate with age. These cross-links are formed by chemical reactions between free amino groups of collagen molecules and reducing sugars (e.g. glucose). This non-enzymatic glycosylation process initiates the Maillard reactions which results in the formation of advanced glycation end products (AGEs) and finally cross-linking between adjacent collagen molecules. Other than enzymatic cross-links these cross-links can form anywhere between the

helical domains of two collagen molecules. Both types of cross-links are shown in Figure 4 below. [21], [23], [24]

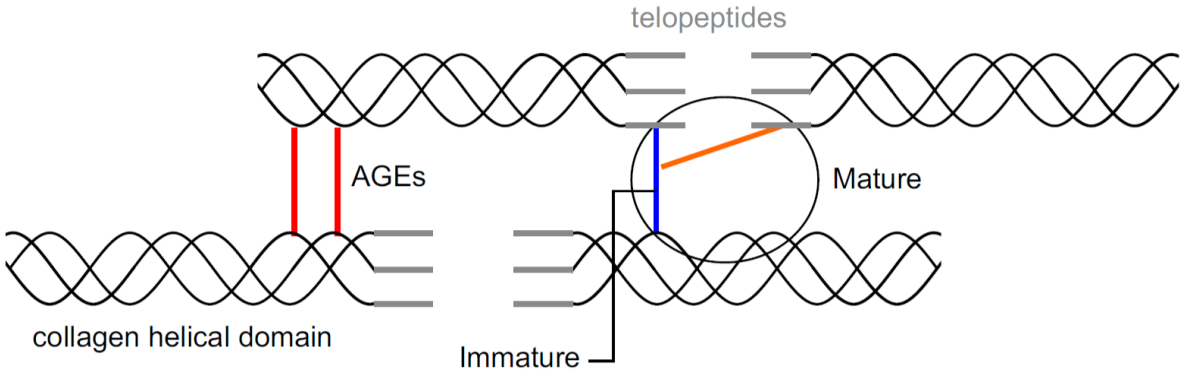

Figure 4: Enzymatic and non-enzymatic cross-links between collagen molecules [25]

2.4 Basic Mechanical Properties of Collagen Fibrils

Depending on their functionality and composition, biological tissues show a wide range of different mechanical properties. Those properties highly depend on the tissue structure at its lowest hierarchical length scale level as it will have the most pronounced overall effect. In general, collagen rich tissues are composite material. Therefore, the characterisation of their mechanical properties can be quite complex. Fibril forming collagens especially, are transversely isotropic materials since the fibrils assemble around an axis in a quasi-hexagonal packing and therefore have differing mechanical properties when the loading direction deviates from the axis. For these fibril-forming collagens, the main contributors to the mechanical properties on the fibrillar level of the tissue are the collagen content, fibril alignment, cross-linking density as well as fibril length and diameter. [26]

By using atomic force microscopy for nanoindentation Wenger et.al. in 2007 [27] were able to determine a reduced elastic modulus of 5 – 11.5 GPa for a single rat tail collagen fibril type I (in air, at room temperature). But, as can be seen in Table 1 below, there is a high variability in the experimental results reported in different studies, depending on the technique and experimental conditions employed.

Table 1: Young´s modulus of collagen fibrils from different experimental studies [27]

Collagen fibril (Ref.)	Technique	State of fibril	Young's mod. (GPa)
Rat tail tendon*	Indentation	Different dehydration states	3.75–11.5
Rat tail tendon (34)	Brillouin	In 0.15 M NaCl solution	9.0
Rat tail tendon (34)	Brillouin	At 30% relative humidity	14.7
Rat tail tendon (34)	Brillouin	At 0% relative humidity	21.5
Rat tail tendon (35)	Brillouin	In 0.15 M NaCl solution	5.1
Rat tail tendon (35)	Brillouin	At 50% relative humidity	11.9
Bovine Achilles tendon (36)	X ray	In 0.15 M NaCl solution	2.9 ± 0.1
Bovine Achilles tendon (17)	Spectroscopy	At 0% relative humidity	2–7
Bovine Achilles tendon (17)	Spectroscopy	In phosphate buffered saline	0.2–0.5
Sea cucumber (13)	Tensile test	In water	12 (high strain)
Sea cucumber (24)	Indentation	<45% relative humidity	1–2
Collagen-like peptide (37)	Simulation	—	4.8 ± 1.0

Note: Harley et al. (34) and Cusack and Miller (35) are spectroscopic measurements performed at hyper-sound frequencies in the GHz range.

For a collagen fascicle, the overall shape of the stress-strain curve is dictated by the cross-linking density. At high cross-linking density, the collagen fibrils behave like hardening springs that will rupture in a brittle manner at their peak stress whereas for fibres with low cross-linking density the energy will dissipate post peak deformations and result in graceful failure [28]. Shown in the Figure 5 below is a typical stress-strain curve for a fascicle which is rich in collagen type I. In the toe region of the curve crimps of the fibril arrangement unfold and the fibrils align parallel to each other. Afterwards the loading on the single fibrils increases, they harden while the backbone structure of the molecules is getting stretched. The molecules slide against each other until first microscopic failure occurs and the fibrils finally rupture.

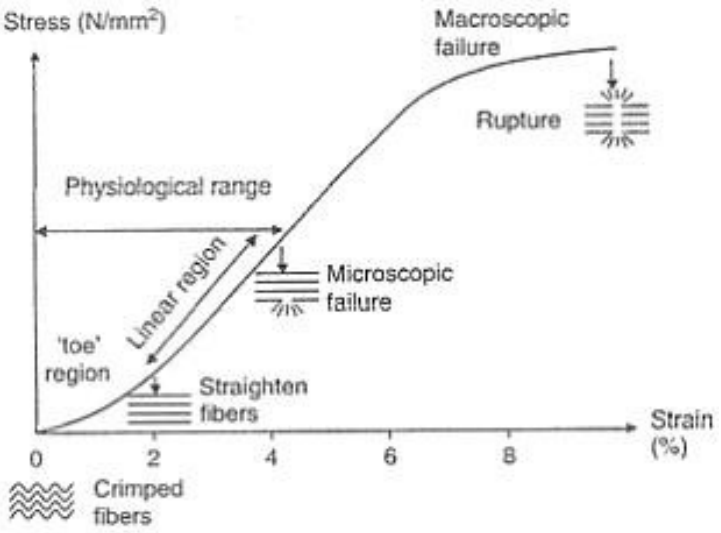

Figure 5: Stress-strain-curve of tendon fascicle [29]

2.5 Collagen During Embryonic Development in Chicks

In 1951 Viktor Hamburger and Howard Hamilton established a new staging series for embryonic development that did not rely on the specific age of the embryo but rather on specific characteristics of its development. The Hamburger-Hamilton (HH) stages sequence the approximately 21 days of chick embryonic development in a series of 46 chronological stages. Beginning with the incubation of the fertilized egg until hatching. In

Table 2 a rough overview of the different stages and developing characteristics is given while in Figure 6 a graphic representation of late embryonic chick development is shown. [30]

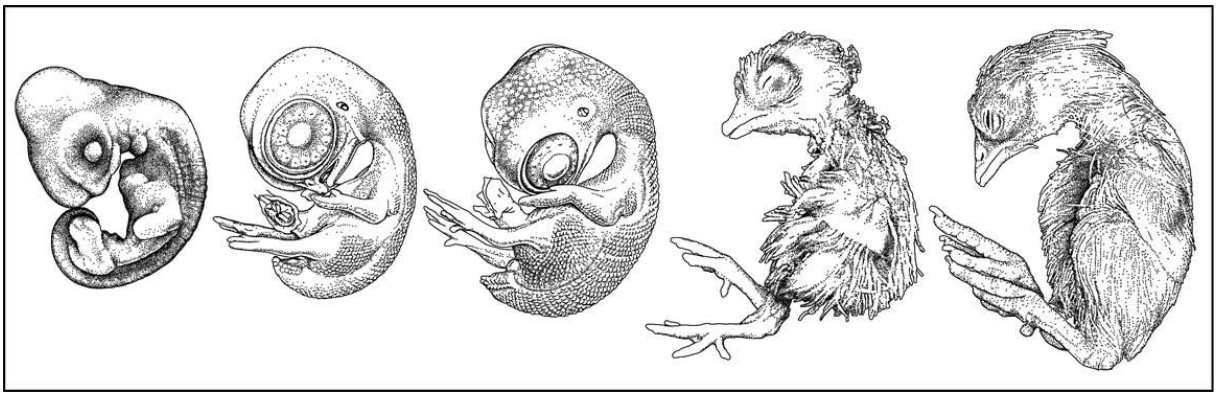

Figure 6: Chick embryo at stages HH25, HH32, HH36, HH40, HH44 from left to right [31]

Table 2: Developing embryonic characteristics at progressing Hamburger-Hamilton stages

HH Stage	Developing Embryonic Characteristics
1-6	primitive streak forms and regresses as the notochord forms in front of it and progresses into the head fold
7-14	somites are visible and neural development begins; blood islands and optic vesicles appear
15-20	the optic cup of the eye, the third branchial arch and cleft are fully formed; the tail bud and extremities start to develop while the amnion closes around the embryo
21-35	species characteristics and limbs become more distinct and form fully; feather germs become visible
36-46	the embryo grows and matures until hatching

The first collagen synthesised during early embryonic development is collagen type IV. It appears in the basal laminae of the ectoderm and endoderm during gastrulation after the formation of the primitive streak at HH3. It later also forms in the notochord, the condensing mesodermal epithelia and the neural tube. The first fibrillar collagen synthesised is of type II

and appears around the notochord. The notochord is an ECM covered epithelial rod that establishes the primary body axis of vertebrate embryos. Besides giving structural strength to the primitive skeletal rod it contributes to mediating the inductive effects of the notochord on growth and differentiation of cells. Collagen type I can first be found around the notochord at HH12 and neural tube at the time of the neural crest formation. [32] These forming fibrils show a diameter of approx. 10 nm and are spread wide in pathways, which are used by mesenchymal cells to migrate. At this stage of embryonic development, collagen I and II provide tensile strength, support adhesion and migration as well as promote differentiation of embryonic cells. [33] The early beginnings of tendon formation are recognisable at HH21 when limb formation becomes more distinct. Tendon formation during embryonic development is typically characterised primarily by molecular markers, ECM composition and ECM organisation. [34], [35], [36], [37], [38] Cells presumably impart mechanical properties to the tendon tissue by secreting, organizing and cross-linking ECM molecules. [39] Cross-linking in tendon during embryonic development has rarely been studies so far. A few studies suggest the contribution of GAG-bridges as well as enzymatic and non-enzymatic collagen cross-links to change mechanical tissue properties during tendon maturation and aging. [40], [41] However, a study by Marturano et al. in 2013 [2] found only weak correlations between elastic moduli of tendon tissue and GAG activity, which supposedly plays a role in regulating collagen cross-links and fibre diameter.

3 Atomic Force Microscope

The Atomic Force Microscope also known as Scanning Force Microscope (SFM) is a high-resolution microscope that was first developed by Binning et al. in 1986 [42]. AFM belongs to the instrument class of scanning probe microscopes (SPMs). Theses microscopes are characterised by a technique that uses a very sharp probe to scan across the surface of a sample. They use the interactions between probe and sample surface to produce a high-resolution image of the sample surface.

3.1 General Principle

The AFM utilises repulsive and attractive forces existing between the surface of a sample and the probe to create a 3-dimensional high-resolution image of the sample surface topography at the nanometre scale.

A sharp probe of the AFM is mounted near the end of a flexible microcantilever arm and raster-scanned across the sample surface. The small and accurate movements of the probe over the surface are facilitated by piezoelectric elements on which the cantilever is mounted. On the upper side of the cantilever a laser light beam is reflected onto a position-sensitive photodetector. Thus, the deflection of the cantilever occurring during movement over the surface can be monitored via the position change of the light beam on the photodetector. From this data, a 3-dimensional image of the surface topography is built up.

3.2 Basic Components

The basic components of a functional AFM are the cantilever and tip to interact with the surface, the piezoelectric transducer to scan the surface and the compartments of the detection method. The following Figure 7 is an illustration of the essential AFM components.

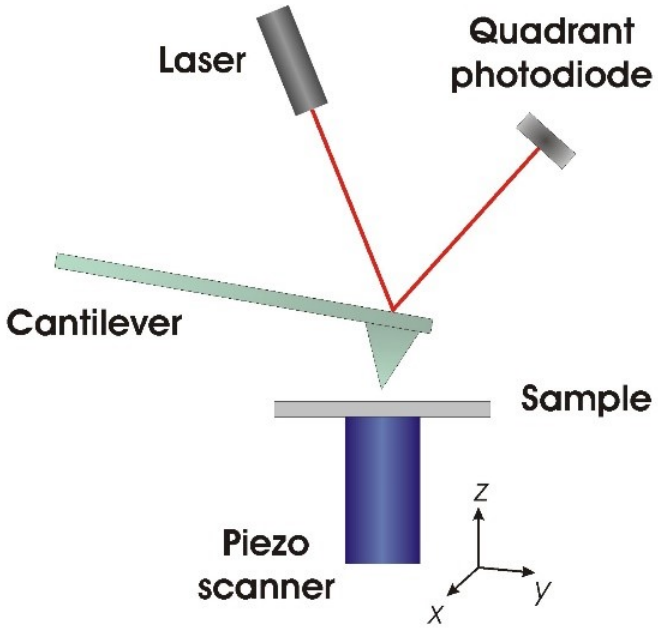

Figure 7: Artistic impression of basic AFM compartments [43]

3.2.1 AFM Cantilever and Tip

There are various shapes and sizes of cantilevers depending on the manufacturer and desired application. A commercially manufactured cantilever is usually made of silicon or silicon nitride. Those materials show a high suitability of mechanical properties such as high yield strength and elastic moduli but depending on the specific application other materials are also possible. Applications with high elastic moduli for example require stiff cantilevers with probes resistant to deformation. But on soft and easily deformed samples an increased force sensitivity and therefore a softer cantilever is required, as of not to damage or deform the sample while scanning. On the upper surface, the cantilever is coated with a thin reflective layer. It is usually made of gold or aluminium to reflect the laser beam onto the photodetector.

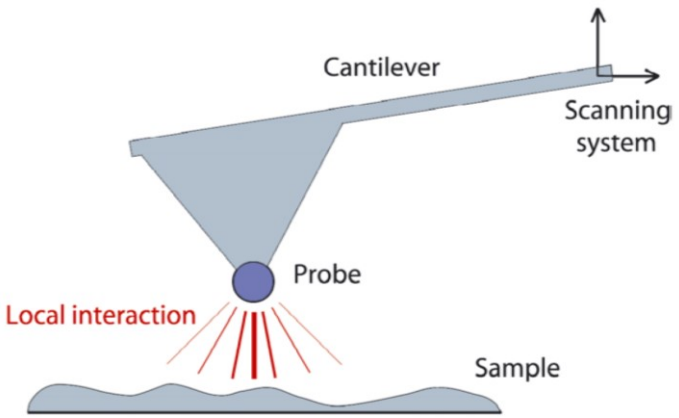

Figure 8: Artistic impression of AFM cantilever [44]

At its free end on the lower surface the cantilever has a sharp tip that acts as the probe for sample interactions (see Figure 8). The tip is commonly formed as a square based pyramid or a cylindrical cone. The shape of the tip is of high importance in determining the physical interactions between the tip and sample, especially for imaging or indentation measurements. The ability of a cantilever to resolve the varying geometric features of a surface topography depends on the sharpness and the aspect ratio of the tip as pictured in Figure 9. The contact area between the tip and sample is a limit to the resolution of the AFM. It depends not only on the sharpness of the tip but also on the force used to press the tip into the surface and the resulting mechanical deformation induced on the tip or surface.

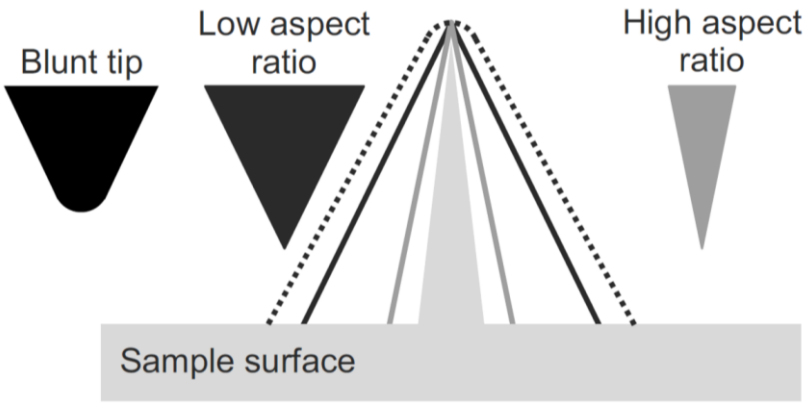

Figure 9: Traces resulting from a blunt AFM tip (dashed trace), low aspect ratio tip (solid black trace) and high aspect ratio tip (solid grey trace) [25]

Furthermore, for steep edges or asperities on a sample surface, that are sharper than the tip, the image of the feature will be based more on the tip shape than the feature. To produce true representation of a surface topography it is therefore necessary to use a sharp tip with a high aspect ratio. [45], [46]

3.2.2 Piezoelectric Transducers

To generate precisely controlled movements of the cantilever, the AFM actuators are made of a piezoelectric material. By applying a small voltage to the actuators, the electrical signal is converted into a physical displacement. The working principle of the AFM scanner relies on the reversion of the piezoelectric effect which describes the generation of a potential difference across the opposite faces of a non-conducting crystal as a consequence of applied external stress.

3.2.3 Detection Method

In general, the detection method of an AFM can be an optical or an electrical method. The AFM used for the experiments described in this thesis utilizes an optical detection method namely light beam deflection. A laser light beam is focused on the back of the cantilever probe and reflected onto a photodetector. This photodetector is a photodiode segmented into four quadrants as shown in Figure 10.

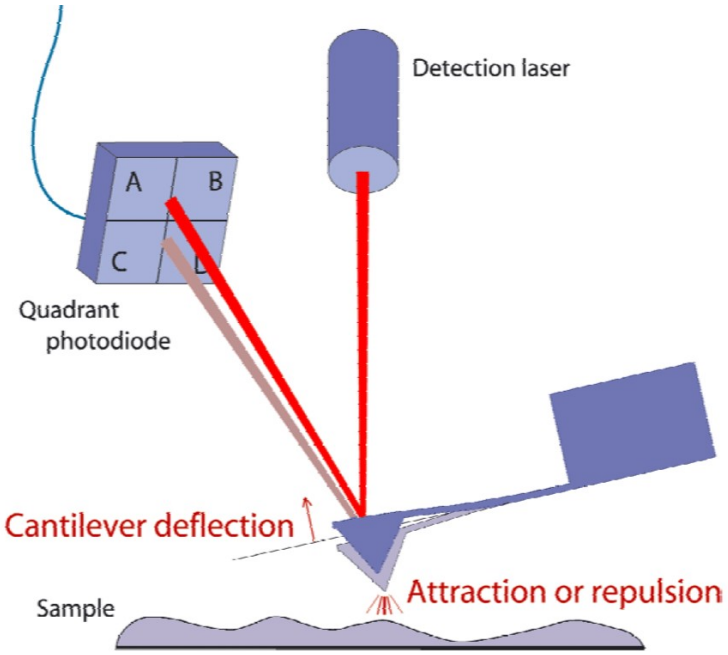

Figure 10: Artistic impression of light beam deflection detection [44]

When a deflection of the probe occurs the laser beam reflection on the photodiode moves and generates a difference in voltage. By using the sensitivity of the cantilever, the voltage difference can be used to calculate the deflection in nanometre as described by the equation below.

$$Deflection = (V_A + V_B) - (V_C + V_D) \quad (1)$$

3.3 Basic Imaging Modes and Feedback Loop Control

There are several different imaging modes and techniques to provide various information about a sample surface when operating the AFM. The choice of imaging mode depends highly on the studied material and its overall surface structure. The following chapter gives a description of the feedback loop control and the most basic imaging modes available to AFM users.

3.3.1 Feedback Loop Control

A feedback loop control is used to keep the motion of an object in a fixed relation to another object. In this case the AFM employs a feedback loop to keep the force acting on the cantilever during scanning at a constant level so that the movement of the cantilever over the sample surface can be executed with high precision.

The interaction force between tip and sample surface can be represented by the Lennard-Jones potential combined with a modified Hertz model. The Lennard-Jones potential calculates the force between a spherical tip and a flat sample as a function of the distance between them as followed:

$$F(r) = k_1 \left[-\left(\frac{\sigma}{r}\right)^2 + \frac{1}{30}\left(\frac{\sigma}{r}\right)^8 \right] \tag{2}$$

Where σ is an interaction parameter, r the distance between the tip and the sample and k_1 is a constant depending on the geometry and material of the tip and sample.

The first term of this model equation shows an attractive component of the interacting forces due to Van der Waals' forces and a repulsive component in the second term. These interactions between tip and sample result in the curve shown below in Figure 11. Because of the nonlinearity of the interaction force curve a feedback control loop is necessary to keep the cantilever at the right distance and in the right force regime during the scanning process according to the imaging mode utilized. [47]

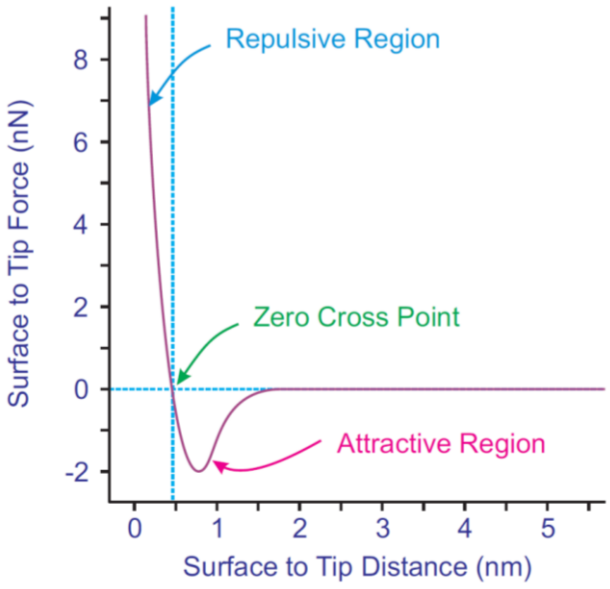

Figure 11: Interaction force between AFM tip and sample surface [47]

The force interactions between tip and sample surface are measured indirectly by monitoring the displacement of the free cantilever end during the scanning process. While operating in contact and intermittent contact mode the vertical deflection and amplitude of the cantilever are monitored respectively. The external disturbance, the magnitude of the measured force interactions, is determined by the setpoint value specified by the AFM user. During contact mode, the feedback loop is used to maintain the specified deflection setpoint at all times. The difference between the deflection setpoint and the actual deflection is measured as the error signal. Through processing this error signal by a proportional-integral-differential (PID) feedback controller the z-piezo transducers are driven to adjust the z-height of the cantilever to minimize the error signal and thus realizing the desired setpoint. [48] [49]

3.3.2 Contact Mode

When operating the AFM in contact mode, the probe remains in contact with the sample surface as indicated in Figure 12. This interaction between the probe and surface is directed by repulsive forces (see Figure 11). While scanning the sample surface, the feedback mechanism is keeping the deflection of the cantilever and the force applied to the surface at a constant level defined by the setpoint.

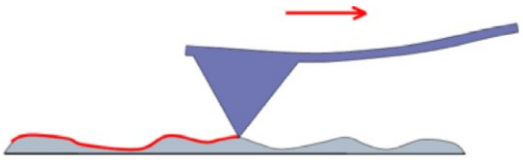

Figure 12: Schematic drawing of cantilever movement (red) during contact mode [44]

This is realized by a change in the z-height of the cantilever which is monitored to create a topographical image of the surface. The contact mode is useful to image relatively smooth surfaces with low lying topographical features as it delivers a high resolution but is prone to the occurrence of lateral forces and sample damage.

3.3.3 Intermittent Contact Mode

During intermittent contact mode, also known as tapping mode, the cantilever is oscillated at a value close to its resonant frequency. When the oscillating cantilever is brought close to the sample, the probe will repeatedly engage and disengage with the surface as shown in Figure 13. This “tapping” motion will restrict the amplitude of the oscillation.

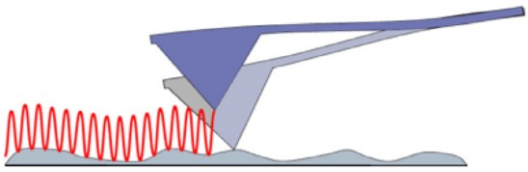

Figure 13: Schematic drawing of cantilever movement (red) during intermittent contact mode [44]

The amplitude will change while scanning due to encounters with different surface features. The feedback mechanism meanwhile aims to maintain a constant amplitude and alters the z-height of the cantilever accordingly. Similar to the contact mode, a surface image is obtained from monitoring these alterations. An advantage of this mode compared to the contact mode is the reduction of lateral forces. But especially for measurements in air, capillary forces due to adsorbed water on the sample surface and adhesive forces have to be taken into account.

3.3.4 Non-Contact Mode

In non-contact mode, the cantilever is again oscillated but at a much smaller amplitude than during intermittent contact mode as can be seen in Figure 14. The cantilever is constantly kept out of contact with the surface and therefore only long-rang interactions, like van der Waals and electrostatic forces occur between atoms in the probe and sample surface.

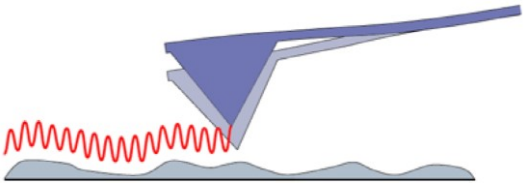

Figure 14: Schematic drawing of cantilever movement (red) during non-contact mode [44]

These forces cause a shift in the frequency of the cantilever oscillation. The detection of this phase shift between the driving and oscillating frequency allows the adjustment of the z-height to keep the cantilever out of contact and is used produces the surface image. [45]

4 Materials and Methods

4.1 Sample Preparation

The collagen samples used for the experiments of this thesis were dissected from the calcaneus tendon of 15 chick embryos in the developmental stages HH37 to HH41 and provided through a collaboration with the University of Rochester. These stages of embryonic development were chosen since a study by Marturano et al. in 2013 [2] found only minimal changes of the mechanical properties in collagen fibrils originating from earlier stages than HH38 and a particular increase in the variation coefficient between samples after HH41. Four of the embryos were injected *in ovo* with a saline solution and two with 15 mg/g β-aminopropionitrile (BAPN) 24 hours prior to dissection at HH40. This was done to inhibit lysyl-oxidase-mediated cross-linking during embryonic development and examine its contribution on the emerging mechanical tissue properties. BAPN binds the active site of lysyl oxidase and therefore inhibits collagen cross-linking. After dissection, the collagen samples were placed directly on glass slides and stored frozen at -80°C until further processing.

To separate the collagen mass from proteoglycans the sample mass on the glass was hydrated with water under a microscope and scraped off the glass slide with tweezers. The mass was then placed in a solution of 1 mg bovine hyaluronidase per 1 ml Sorensen´s buffer (0.1M with pH-7.4) and incubated at 37°C for 24 hours. After incubation, the collagen was smeared out with tweezers on a Polysine® coated glass slide to reveal single collagen fibrils. Further rinsing with deionized water removed all remaining proteoglycans and salts. Again, the dried samples were stored frozen at -80°C until further testing.

4.2 Atomic Force Microscopy

The AFM used in this thesis to image and characterize the surface of collagen samples in air and liquid was manufactured by JPK Instruments and of the model NanoWizard 3. The cantilever of choice was the type 4XC-NN from OPUS with a resonance frequency of 17 kHz and 0.3 N/m nominal spring constant, according to manufacturer which is shown in Figure 15 below.

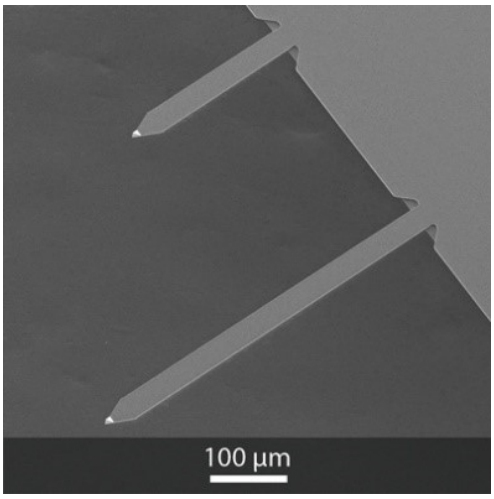

Figure 15: SEM image of OPUS 4XC-NN cantilevers (short cantilever: 75kHz, 2.5 N/m ; long cantilever: 17kHz, 0.3 N/m) [50]

As some of the experiments were done in contact mode a stiffer cantilever might have damaged the sample surface and delivered a low-resolution image. Also, this cantilever was chosen to match the stiffness of collagen to optimise the sensitivity and signal-to-noise ratio.

4.2.1 Calibration Procedure

All AFM experiments were executed in a temperature-controlled room at approx. 24°C. Prior to the experiments calibration of the cantilever was performed for each sample.

Firstly, the cantilever sensitivity was determined by recording a 4x4 force map on a mica calibration sample in air as well as later in PBS (10mM with pH-7.4) on glass. By monitoring the deflection and z-displacement of the cantilever during force mapping 16 deflection vs. z-displacement curves were produced. An example curve is plotted in Figure 16. The cantilever sensitivity equals the inverse slope of the retract signal. From all 16 curves the mean cantilever sensitivity was calculated first in air later again in PBS.

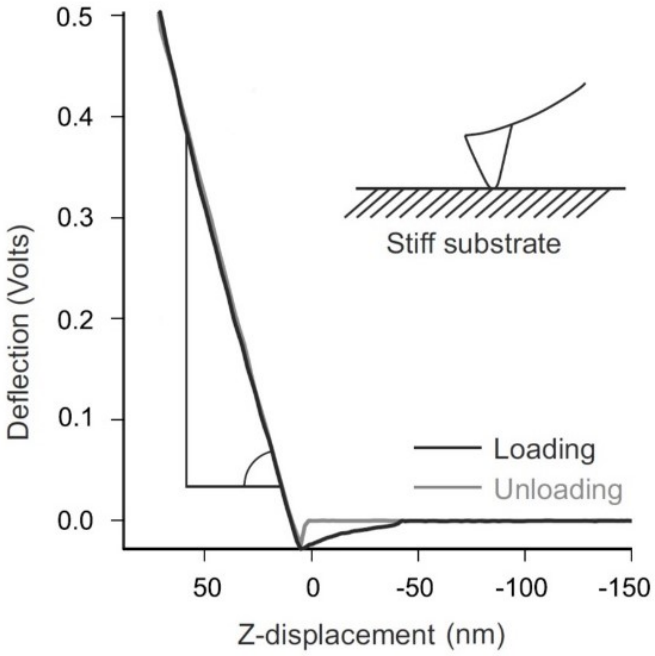

Figure 16: Deflection vs. displacement curve when the cantilever is brought into contact with the sample [25]

The mean of the inverse slope gradients gave the sensitivity of the cantilever. The sensitivity varied for each cantilever but to give reference values, in air and PBS it was measured at 66 ± 9 nm/V and 55 ± 4 nm/V respectively. The cantilever sensitivity is an important conversion parameter that can be used to convert the deflection unit from volt into nanometres as shown in the equation below.

$$Deflection\ [nm] = Cantilever\ Sensitivity\ \left[\frac{nm}{V}\right] * Deflection\ [V] \qquad (3)$$

Since commercial cantilevers show a wide variation, the spring constant (see Figure 17) had to be determined experimentally for every cantilever. This was done by using the thermal noise method proposed by Sader et al. in 1999 [51]. To determine the spring constant, the cantilever is oscillated away from the surface where it is affected by small force impulses. These small fluctuations are measured by the AFM and used to assert the spring constant. The spring constant values were measured at 0.25 ± 0.06 N/m.

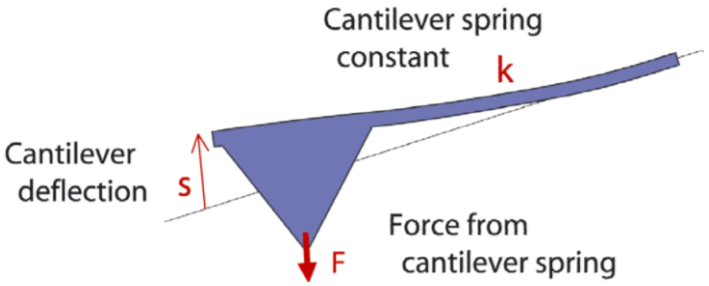

Figure 17: Artistic impression of cantilever as a spring

As the tip geometry of a cantilever is a limiting factor for the quality of indentation results, the tip shape had to be determined. The tip radius of the cantilever can be obtained by imaging a calibration sample that consists of an array of sharp cones with known geometry.

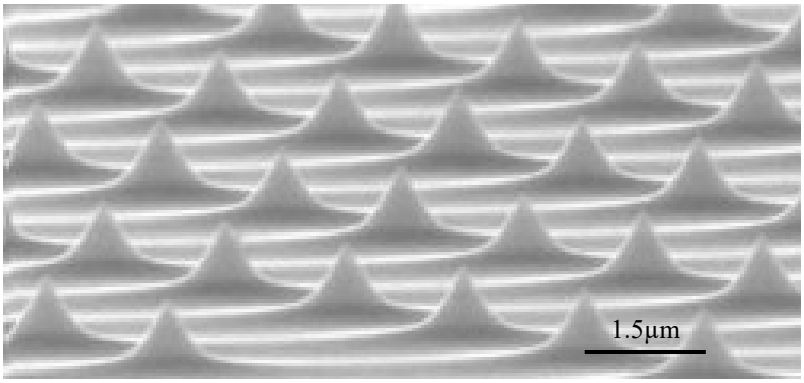

Figure 18: SEM image of TGT1 grating by NT-MDT [52]

This calibration sample imaged in Figure 18 is a tip characterization grating TGT1 by NT-MDT formed on a silicium wafer top surface. The radii of the grating tips and the cantilever tip are in the sample size range (≈ 5 nm) so that a mathematical deconvolution of the AFM tip is necessary to determine its radius based on the AFM height image. [27]

4.2.2 AFM Imaging

After the calibration procedure, a sample location with a high probability of multiple single collagen fibrils being present is chosen by optical light microscopy for imaging (see Figure 19). The AFM imaging is done in air and by operating in contact mode. The contact mode is chosen for imaging since the collagen fibrils are small, low lying features and to get high resolution images. Lateral forces had to be monitored carefully during contact mode. Firstly, an overview image of the location is taken with the AFM (see Figure 19) to guarantee the presence of at least 7 single collagen fibrils and some images of interesting collagen structure if present.

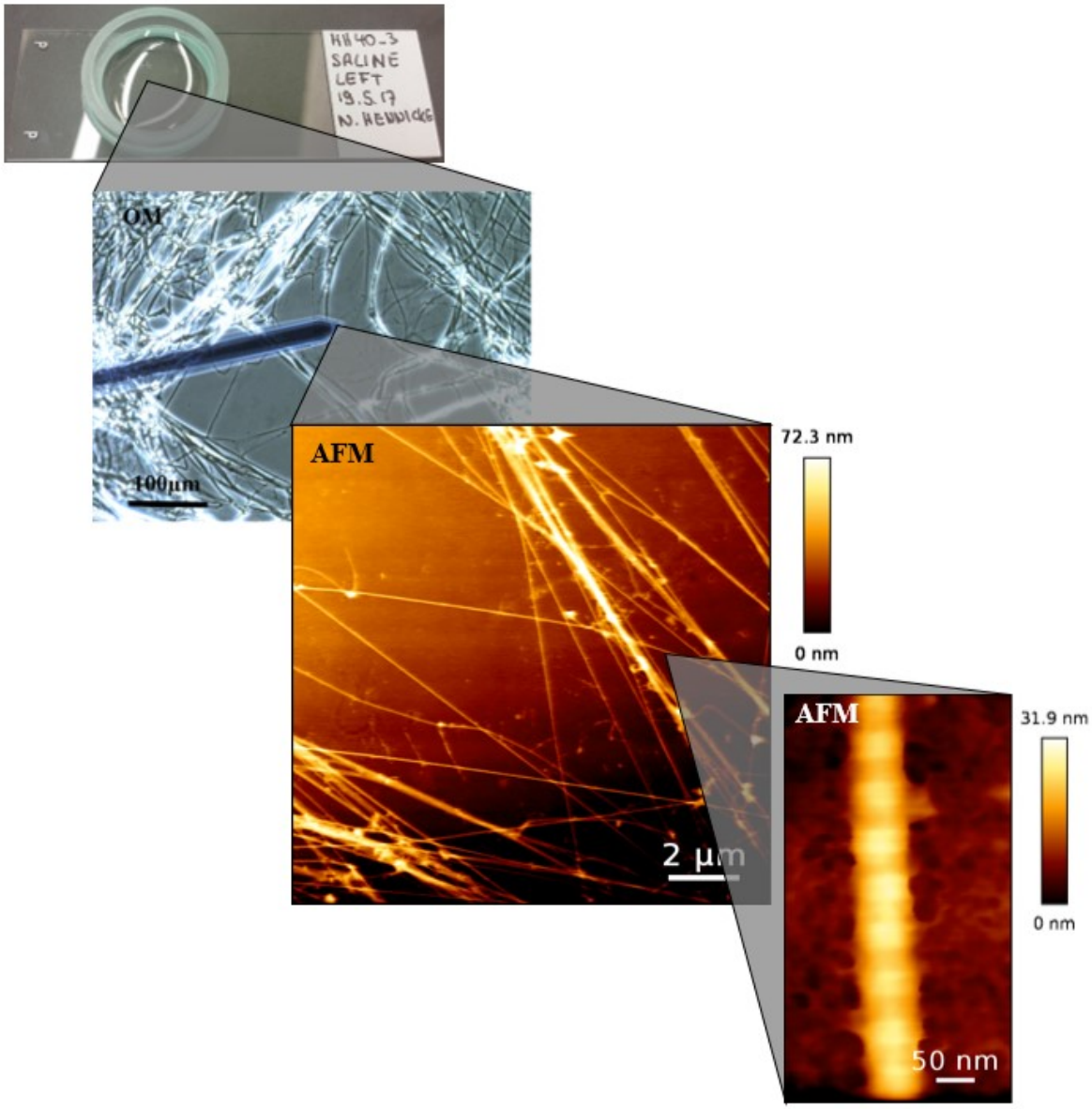

Figure 19: Collagen sample in PBS at different magnification stages (HH40)

Afterwards, a region of interest (ROI) is selected that includes a fibril section and a portion of the glass slide (see Figure 19). The ROI is imaged with the scanning direction perpendicular to the fibril. AFM imaging in air using contact mode allows the discrimination of individual collagen fibrils from fibril bundles as is shown in Figure 20. This knowledge is essential for further nanomechanical experiments on hydrated single fibrils under physiological conditions in PBS.

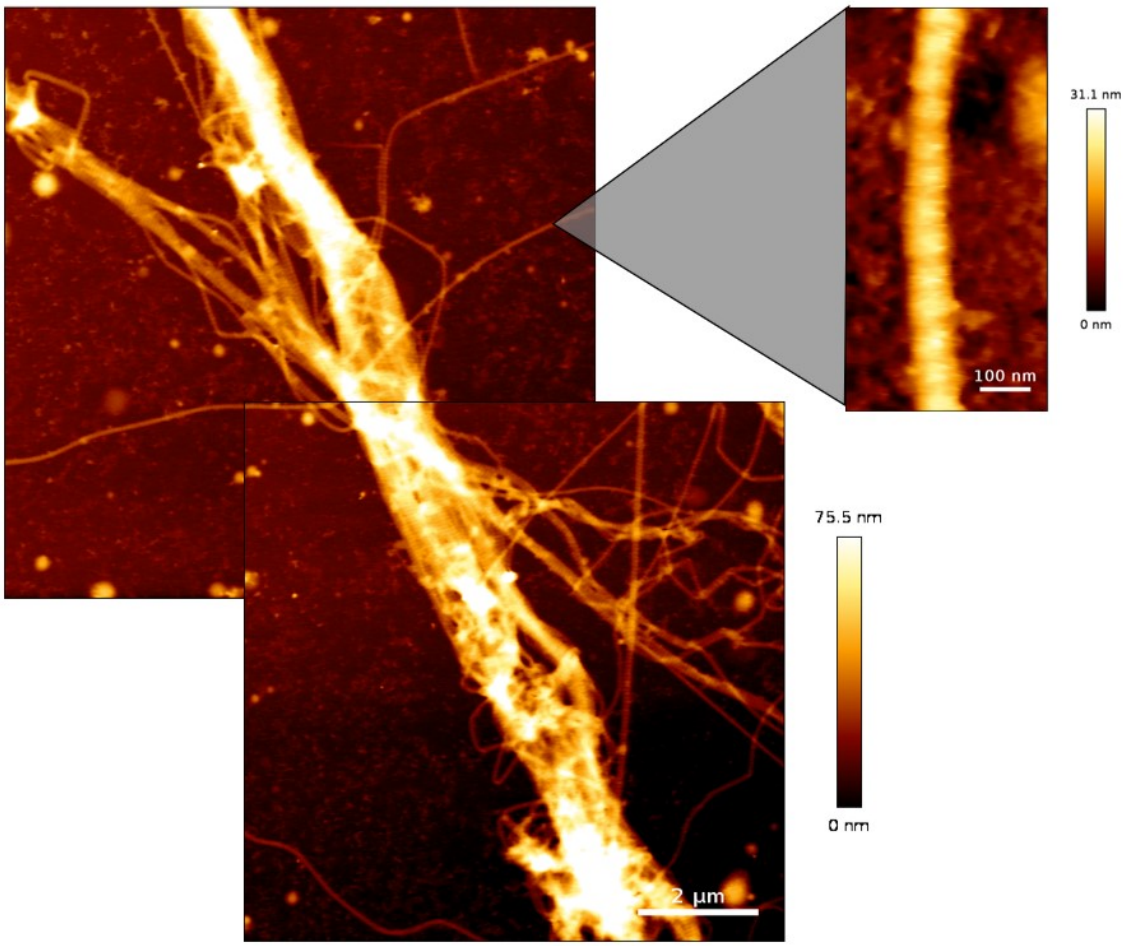

Figure 20: AFM height image of crossing collagen fibril bundles with side shoots of single collagen fibrils (HH40)

4.2.3 Cantilever-Based Nanoindentation

Prior to the indentation experiments on single collagen fibrils the cantilever sensitivity was measured on the glass slide in PBS. Although the location of collagen fibrils on the glass slide was determined by AFM imaging in air (see chapter 4.2.2 AFM Imaging), a location overview in PBS had to be recorded to account for thermal drift. To avoid artefacts, that occur while using contact mode in liquid, this was done by quantitative imaging (QI^{TM}).

The QI^{TM} mode, similar to the force mapping mode, is a force-curve-based imaging mode. It records a 20 µm x 20 µm image with 256 x 256 pixels at regular imaging speed while recording a complete force distance curve at every pixel. This mode works in fluids and on soft materials since the cantilever does not scan the sample surface but approaches the sample and retracts before moving to the next position. As the QI^{TM} mode operates with a movement algorithm that prevents lateral forces and controls vertical forces there is no need for a setpoint or gain

adjustment while imaging. Figure 21 shows that the QI™ mode delivers a high-resolution force map and a corresponding slope map of the image.

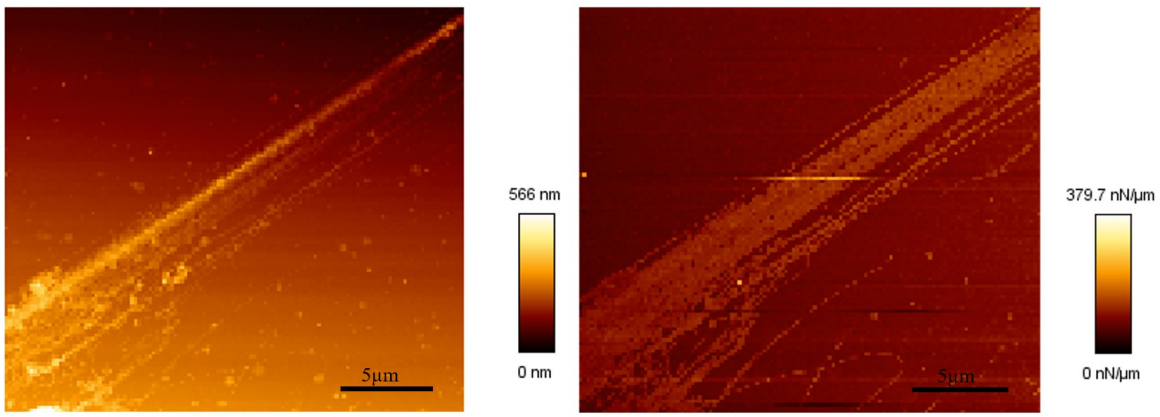

Figure 21: QI™ results *left:* force map; *right:* slope map

The indentation experiments on single collagen fibrils were performed in force mapping mode. By operating the AFM in this mode an indentation experiment is performed on each pixel of the image but slower than in the QI™ mode. Through pixel-by-pixel analysis of the resulting force curves a force volume (FV) map is created. During cantilever-based nanoindentation the tip of the AFM cantilever is used to indent a biological tissue. Compared to conventional nanoindentation the tip used in cantilever-based nanoindentation shows a lower contact area function and the ability to detect several nanometres of deflection. The AFM tip indents the surface at a predefined loading rate until the maximum deflection of the cantilever is reached. Afterwards the tip retracts and the deflection is removed. During the procedure the vertical deflection and the displacement in z-direction of the cantilever is recorded. By using Hooke's Law, the force is calculated and a force-displacement curve created. The equation is shown below with k being the spring constant and s the deflection of the cantilever.

$$F = -k * s \tag{4}$$

In classical mechanics the elastic modulus of materials is normally derived from tests of compression or tension. However, the loading performed by cantilever-based nanoindentation is not considered uniaxial. Due to the structural anisotropy of collagen fibrils the resulting elastic modulus is a contribution of the compressive transvers and tensile longitudinal elastic modulus. Therefore, the elastic modulus of collagen fibrils tested via cantilever-based nanoindentation will be referred to as the indentation modulus during thesis.

For indentation experiments on thin samples like collagen fibrils, the effects of the sample substrate on the measurements have to be considered. To avoid any substrate effects but at the

same time ensure sufficient cantilever deflection the maximum indentation depth is limited to 10% of the total sample thickness according to Buckle's rule and Andriotis et al. [23]. By applying varying loads to single fibrils and comparing maximum indentation depth, fibril height and derived indentation modulus, an indentation load of 0.5 nN was chosen empirically. As the fibrils were indented with a predefined load, the indentation depth was not controlled during indentation. The ROI for the experiments is chosen similarly to the images taken in air. An example of a force-map taken in PBS is shown in Figure 22. Each pixel of the force-map represents a force-indentation curve as is illustrated below. The curve plot shows the z-displacement of the AFM head on the horizontal axis. The cantilever moves downward on the sample until its vertical deflection reaches the load defined by the setpoint.

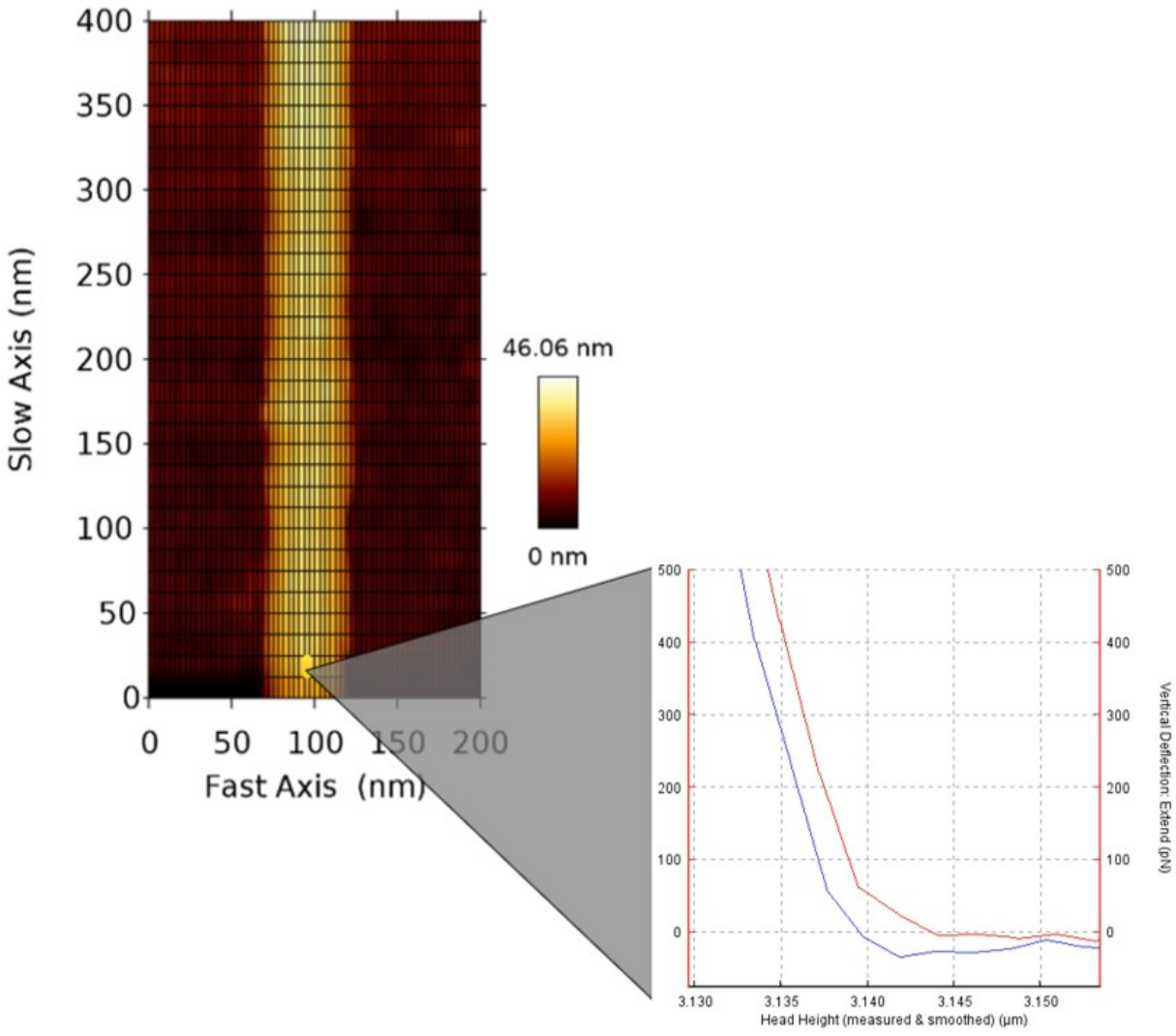

Figure 22: Force map of single collagen fibril HH37 in PBS with force-indentation curve (*blue:* retract; *red:* extend)

The exact size of the ROI depends on the pixel resolution of the FV map. To minimize thermal drift during the experiments the recording time and therefore the resolution is kept low. For the later calculations of an accurate indentation modulus, the indentation curves used for the

calculations need to be measured on the crest of the collagen fibrils. Indentation curves taken on the side of a collagen fibril tend to differ due to the errors associated with improper contact between tip and sample. It was found empirically that a minimum of 10 lines per fibril width are needed to record the required data on the fibril crest. This delivers approx. 20 to 40 force-indentation curves from the fibril crest depending on the exact length of the ROI (see summary of sample sizes in appendix).

4.3 Data Analysis

4.3.1 Fibril Diameter

Deep indentation of the tip may result in plastic deformation of the sample during loading. To avoid plastic deformation and influences of the substrate material on the sample stiffness Buckle's rule is considered. It states, that the indentation depth should not exceed 10% of the sample thickness. The surface structure of single collagen fibrils is mainly characterized by the typical D-banding which is shown in Figure 23. This typical structure is the result of peak and trough regions on the fibril surface. The diameter difference between peak and through features can be measured to be around 3 nm on fibrils in air.

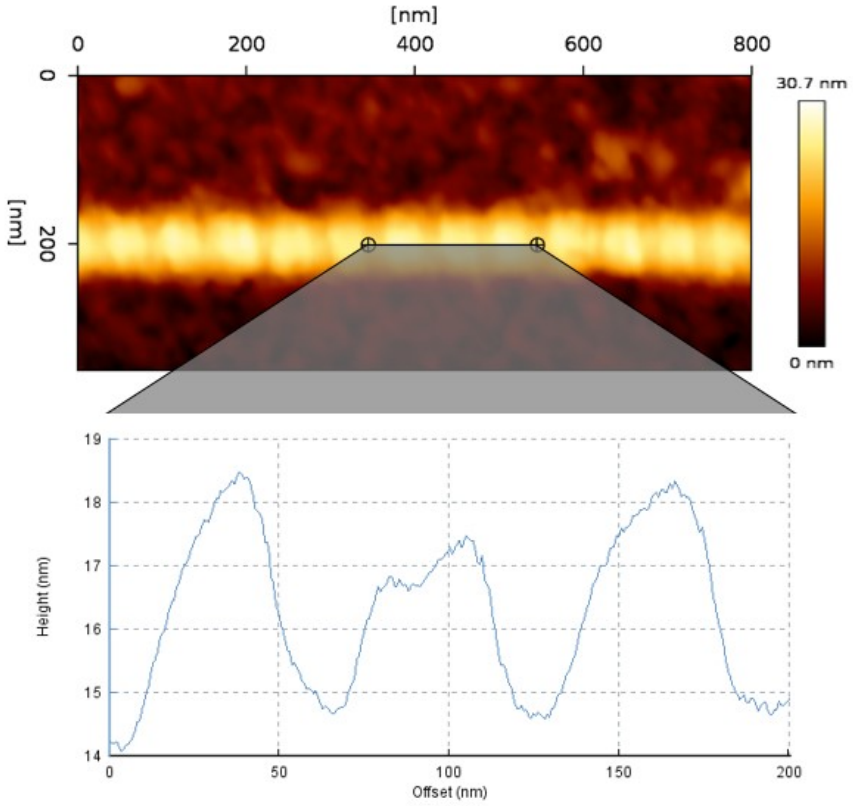

Figure 23: D-banding of single collagen fibril HH38 in air

To ensure indentations depths within the safety range defined by Buckle's rule and for further calculations, the mean diameter d of the fibrils in PBS and air is determined. Firstly, the raw force map data which contains the height image of the collagen fibril is corrected by applying a median filter. The retrace plane of the height image is levelled to remove any tilt of the substrate glass slide by plane fitting.

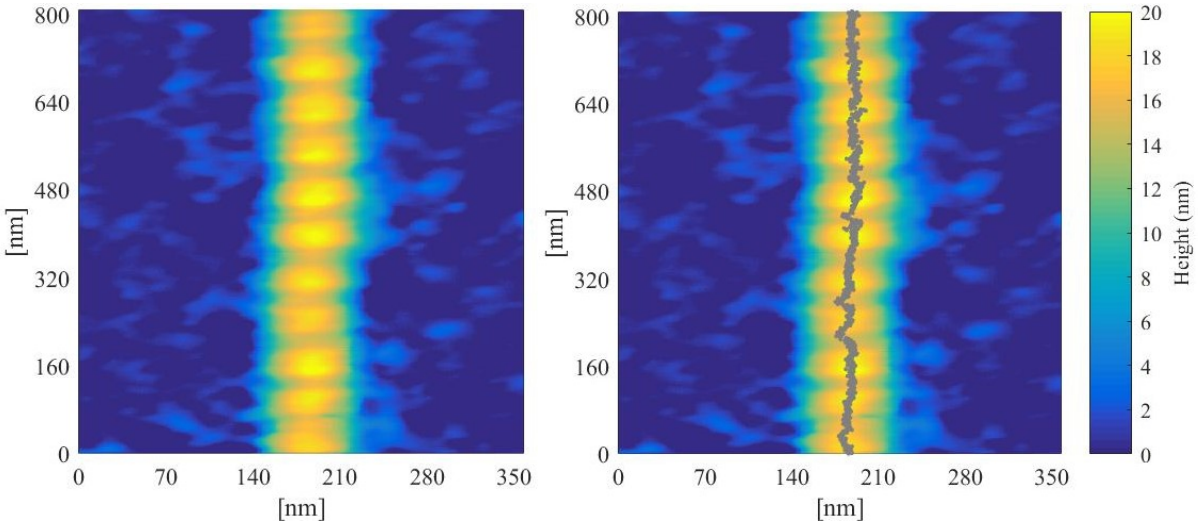

Figure 24: Height image of single collagen fibril stage HH38 *left:* raw data; *right:* processed data with maximum height values within ROI

Afterwards, the data values are converted to the nanometre scale and a region of interest which encompasses the collagen fibril is selected. Within the selected ROI the maximum height value of every image line is calculated as shown in Figure 24. The average fibril diameter is then calculated by using the maximum fibril height of each cross-section line. The diameter data of the fibrils imaged in air can be obtained from the height image with the same technique.

4.3.2 Hydration of Collagen Fibrils

Various studies on collagen fibrils under bulk aqueous solution have shown a reduction in elastic modulus compared to anhydrous form of the fibrils [26], [27]. Figure 25 shows a single collagen fibril at development stage HH 41 imaged dehydrated in air and after hydration in PBS. Cross-sections on both height images show a definite increase of the fibril diameter in the hydrated state. Therefore, the data on the fibril diameter is also used to determine the swelling ratio resulting from the mean diameter increase caused by hydration.

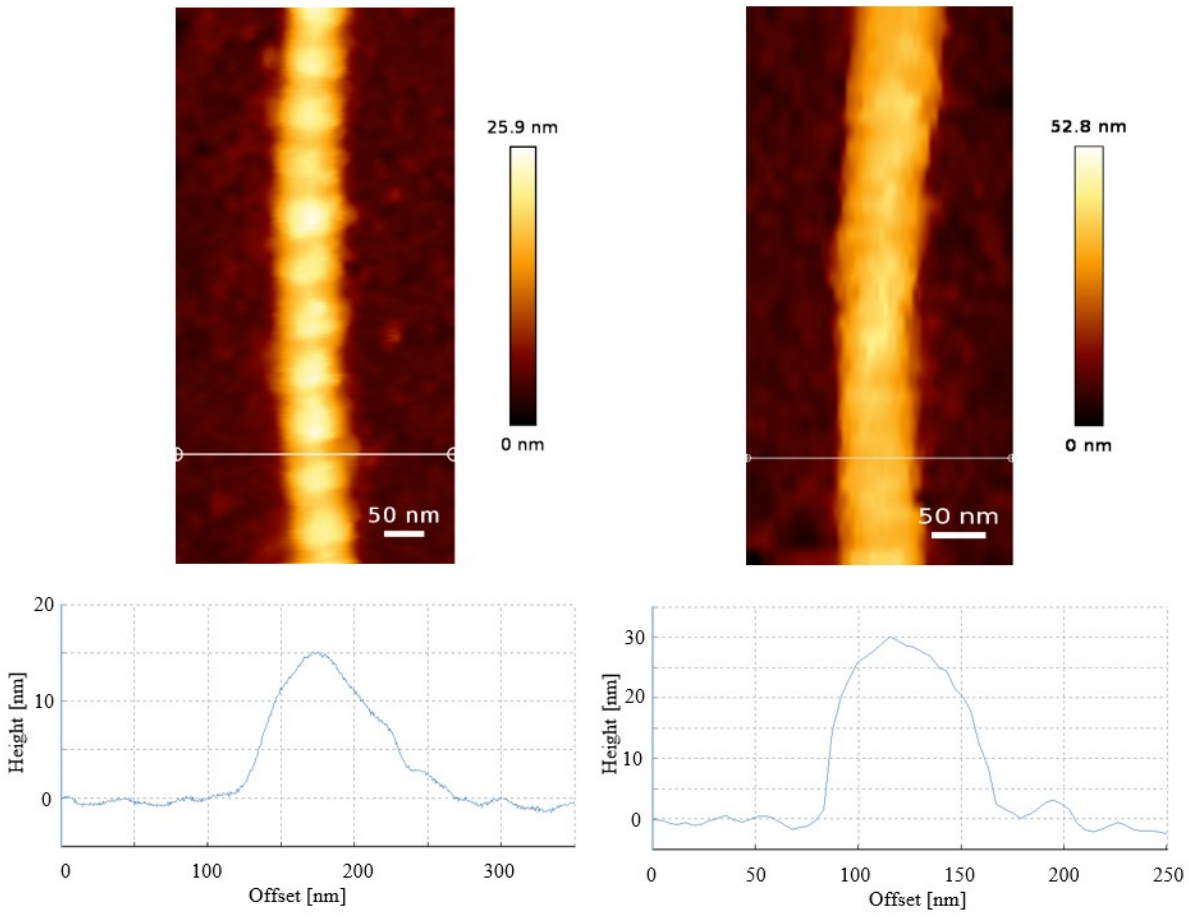

Figure 25: Cross-section on height data of single collagen fibril at stage HH41 *left*: in air; *right:* in PBS

All fibrils were imaged under dry conditions in air and indented under physiological conditions in PBS. When hydrated collagen fibrils absorb water from the PBS solution, the distance between single collagen molecules increases and the fibril swells. The swelling ratio can be calculated using the mean fibril diameter in PBS and air as shown below.

$$Swelling\ Ratio = \frac{d_{PBS}}{d_{air}} \tag{5}$$

4.3.3 Elastic Modulus of Collagen Fibrils

There are a variety of contact mechanics models that can be used to extract the indentation modulus from force-indentation data. In this thesis the Oliver and Pharr model [53] was chosen. To determine the elastic modulus of a single collagen fibril a post analysis of the derived force curves is required.

Calculations:

During indentation two solid bodies are brought into contact with each other and are subjected to elastic deformation. Mathematically this is expressed with the following equation:

$$\frac{1}{E_r} = \left(\frac{1-\nu_i^2}{E_i} + \frac{1-\nu_s^2}{E_s}\right) \tag{6}$$

with ν being the Poisson's ratio and E the elastic modulus of the intender (index i) and the sample (index s). E_r is the reduced modulus of the combined system and is also known as the indentation modulus. In cantilever based nanoindentation the AFM tip is used as an indenter and is much stiffer that the collagen sample ($E_i >> E_s$). Therefore, the indentation modulus is only determined by the samples elastic modulus and its Poisson's ratio. [27]

$$\frac{1}{E_r} = \frac{1-\nu_s^2}{E_s} \tag{7}$$

The Oliver and Pharr method is used to determine E_r directly from the unloading force-displacement curves of the force map. An example force-displacement data set from an indentation experiment is illustrated in Figure 26. Only the unloading curves from the recorded data are used for the analysis to avoid plastic contributions.

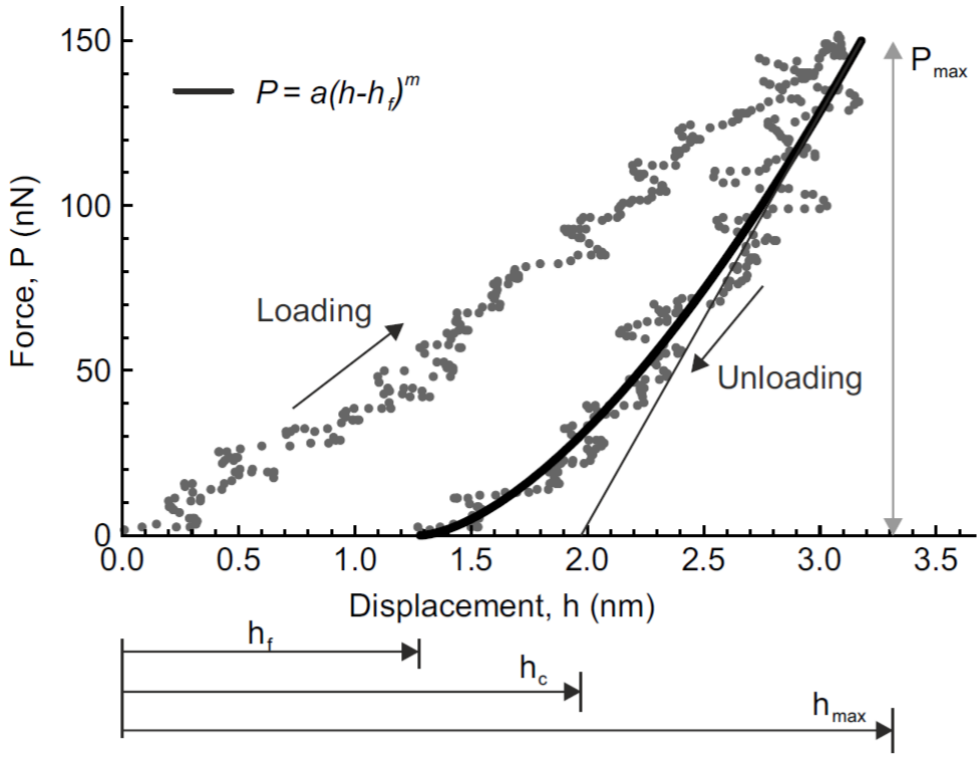

Figure 26: Schematic illustration of a force-displacement data set from an AFM cantilever-based nanoindentation experiment [23]

Firstly, the data of the unloading curve is fitted by using the approximation of the unloading curve described by the following equation:

$$P = a\left(h - h_f\right)^m \tag{8}$$

In this equation P represents the indenter load, h the vertical displacement of the indenter, h_f the final indentation depth and m as well as a are fitting factors. The applied load is also expressed by Hooke's law ($P = -k_C D$) which uses the cantilever stiffness k_C and deflection D. The fitted unloading curve is indicated in Figure 26. By subtracting the cantilever deflection from the z-displacement data the measurements of the tip indentation are provided.

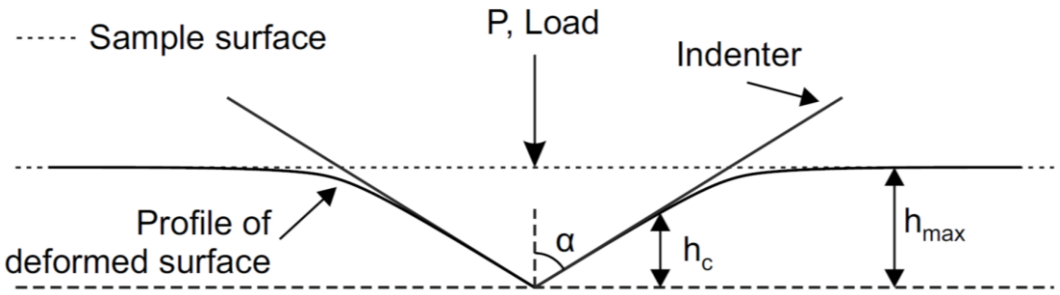

Figure 27: Schematic drawing of a cantilever tip indenting a flat surface [25]

The depth at which contact between the sample and indenter is made during indentation is defined as the contact depth h_C (see Figure 27).

$$h_C = h_{max} - \varepsilon \frac{P_{max}}{S_C} \tag{9}$$

Here, h_{max} is the maximum indentation depth, S_C the contact stiffness of the collagen fibril at maximum indentation depth and ε a constant that depends on the indenter geometry. ε can be determined by using the following relationship with the exponent m and the Gamma function Γ:

$$\varepsilon(m) = m\left[1 - \frac{2\Gamma(\mathrm{m}/2(\mathrm{m}-1)}{\sqrt{\pi}\Gamma((1/2(m-1)))}(m-1)\right] \tag{10}$$

According to the experiments of Oliver and Pharr this leads to the following calculation of the reduced modulus:

$$E_r = \frac{1}{\beta}\frac{\sqrt{\pi}}{2}\frac{S_C}{\sqrt{A_C(h)}} \tag{11}$$

Where β is a dimensionless parameter that varies depending on the indenter shape. By substituting this equation 11 into equation 7 the elastic modulus of a single collagen fibril can be determined.

$$E_S = \frac{1}{\beta}\frac{\sqrt{\pi}}{2}(1-\nu_s^2)\frac{S_C}{\sqrt{A_C(h)}} \tag{12}$$

This final equation requires the determination of the projected area of contact A_C during indentation, the contact stiffness and the Poisson's ratio of collagen.

Projected Area of Contact:

The projected area of contact is dependent on the size and shape of the indenter which in this case is the AFM tip. The tip radius R is obtained by utilizing the AFM image of the characterisation grating TGT1 (Figure 28). As the radii of the grating tips and the AFM tips are in the same size range and the performed indentation depths were smaller than R, a mathematical deconvolution was performed.

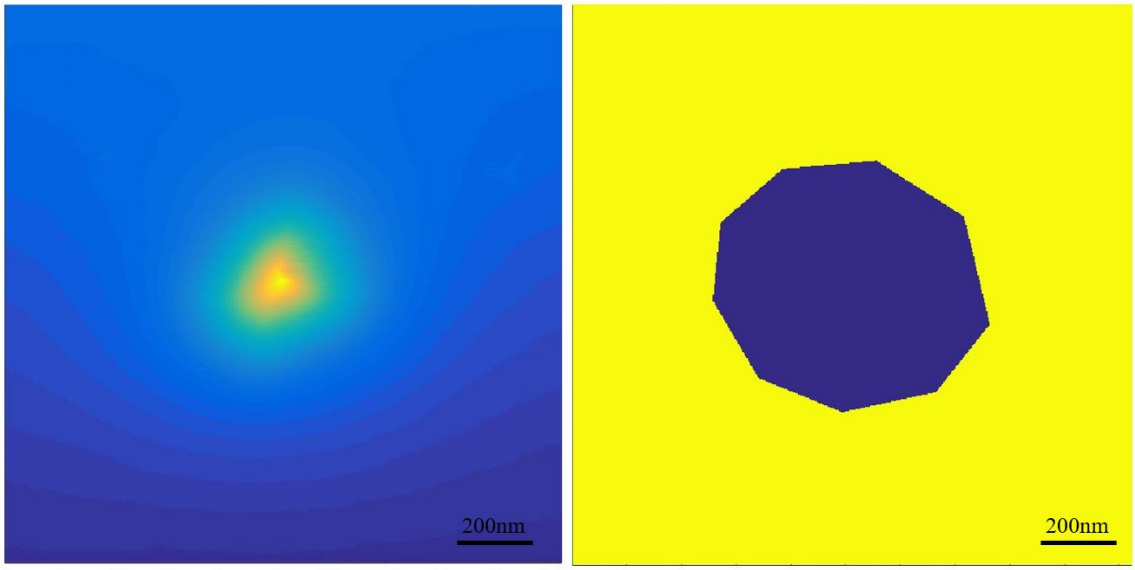

Figure 28: *left:* AFM height image of TGT1 cone with applied median filter; *right:* binary mask of selected deconvolution area

The AFM tip apex is assumed to be spherical and its radius is determined by using the AFM height image of the TGT1 grating. Through subtraction of the grating parameters (given by the manufacturer) from the AFM tip radius estimate, the AFM tip apex is reconstructed. The grating tips are assumed to be cones with tip radii of 5 nm and an opening angle of 50 degrees. To generate an image of the AFM tip, as shown in Figure 29, a reconstruction algorithm programmed in Matlab R2015b was applied. [27], [54]

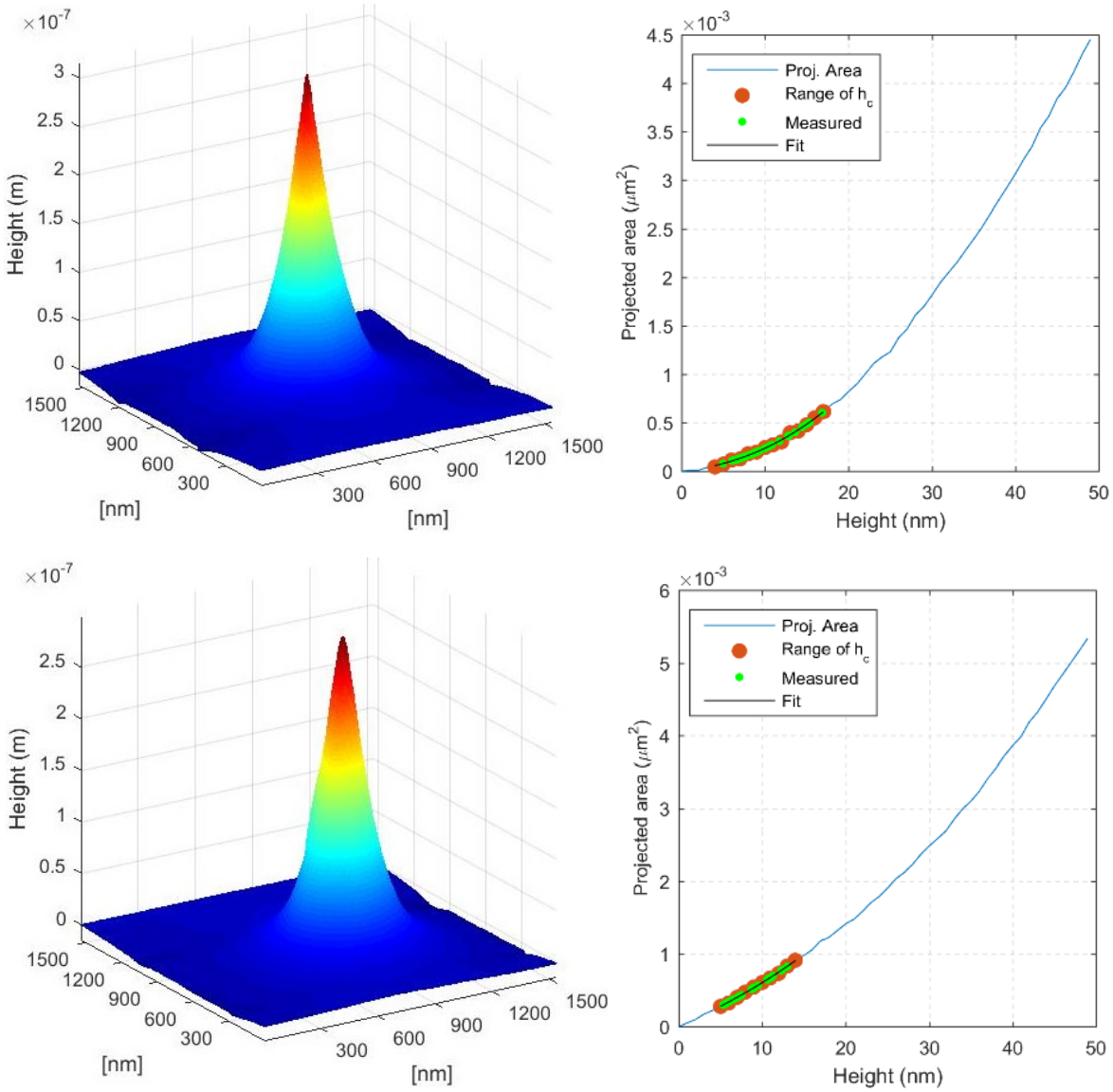

Figure 29: *Left*: two three-dimensional height images for AFM tip reconstructions of different cantilevers model OPUS 4XC-NN; *Right:* corresponding projected area function of the reconstructed tip image

Because of the high aspect ratio of the 4XC-NN cantilever tip, the area of contact is expressed with the second order polynomial as followed:

$$A_C(h) = ah^2 + bh \tag{13}$$

Where A_c is the projected area in µm², h is the height and a as well as b are fitting parameters.[23]

Contact Stiffness:

The true contact stiffness values of every single collagen fibril are obtained by correcting the upper 75% of the indentation curve with a reference slope that indicates the cantilever stiffness. The fitting of the curve to the reference slope improves the signal to noise ratio distinctively and subsequently increases the accuracy level of the indentation modulus calculations. Figure 30 shows a sample of an indentation curve with a reference slope.

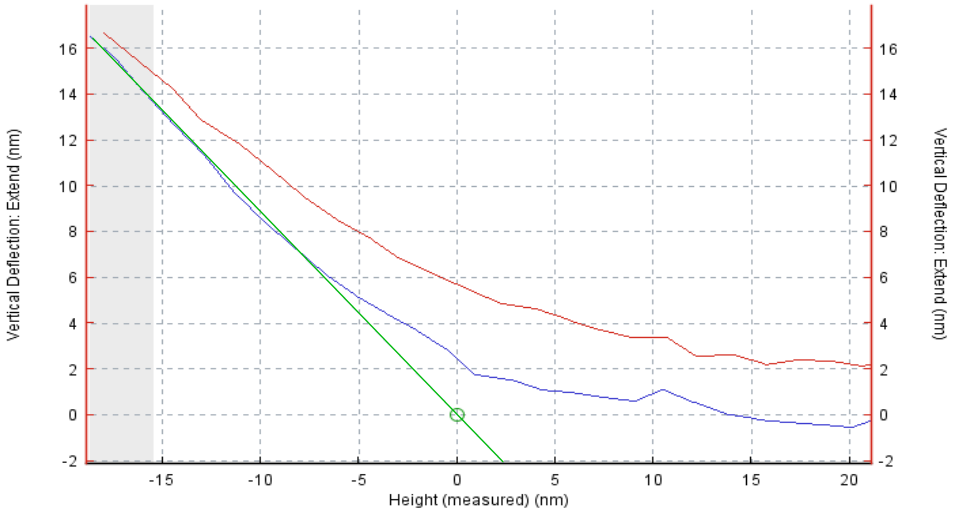

Figure 30: Indentation curve (*blue:* unloading curve; *red:* loading curve) of collagen fibril at HH40 with reference slope (*green*)

This reference slope is a calculated mean of at least 10 unloading curves taken on the glass substrate next to the fibril as illustrated by the white frame in Figure 31.

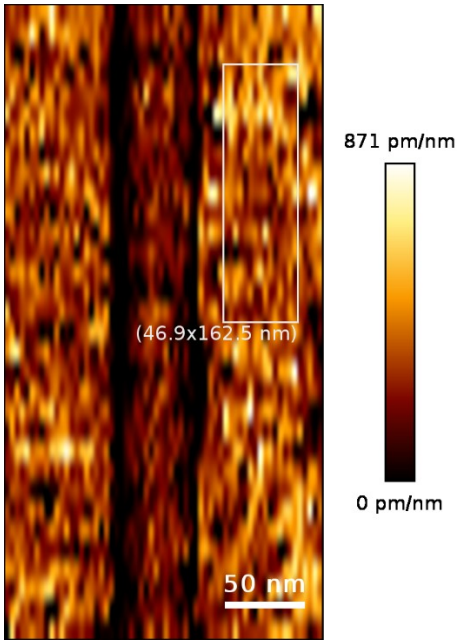

Figure 31: Slope of fibril force-map HH37, *white inset:* locations indicating curves that were used to calculate the mean reference slope

Poisson's Ratio:

The exact Poisson ratio of collagen is unknown. However, solid materials typically have a Poisson's ratio between 0 and 0.5 which delivers a lower and upper limit for the elastic modulus. In this thesis a Poisson ratio of 0.5 is assumed for all fibril calculations.

By using the described mechanical theory and equations, the elastic modulus for each collagen fibril is calculated. For time and repeatability purposes the fibrils were processed by using the JPK data processing software and post-processed by using a Matlab script provided by the ILSB Institute of the Technological University Vienna.

4.3.4 Statistical Analysis

The number of sample embryos, fibrils and indentation curves analysed is summarized in the appendix. All statistical analyses were performed in PAST Version 3.19 (Hammer et al. 2001, University of Oslo).

Normality of distribution was tested with the Shapiro-Wilk test. For normally distributed groups Levene's test was performed to test for differences of variances with continued analyses of variances or Welch-t-test. To subsequently determine significant differences between groups Tuckey's pairwise test was employed as a post hoc.

In case of rejected normality Kruskal-Wallis test was used to test for equal medians between groups. Significant differences between populations were afterwards determined by using Dunn's test with Bonferroni correction as a post hoc.

To measure rank of correlations Spearman's rank correlation coefficient (r_s) was calculated. Results were considered to be significant for p-value < 0.05.

5 Results

5.1 Collagen Fibril Mechanics During Embryonic Development

5.1.1 Indentation Moduli of Collagen Fibrils

The analysis of typical force-indentation curves with an applied force of 0.5 nN resulted in the calculation of a mean indentation modulus for each single collagen fibril tested. The results of the nanoindentation experiments on collagen fibrils at different embryonic development stages between HH37 and HH41 are represented in Figure 32.

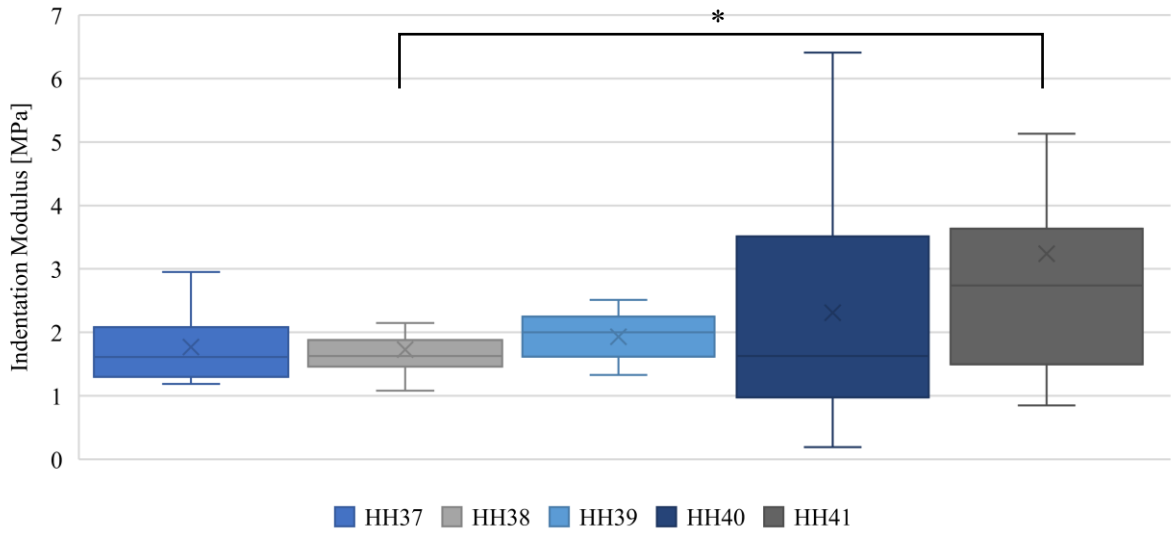

Figure 32: Indentation moduli for collagen fibrils at development stages HH37 to HH41 shown as median (line), mean (x), interquartile ranges (boxes) and range (whiskers); Statistical indicator: * = $p < 0.05$

The resulting data was analysed statistically with the Shapiro-Wilk test regarding normality of the distributions. However, the null hypothesis of normality had to be rejected ($p < 0.05$) for the indentation moduli distributions at HH38, HH40 and HH41. Therefore, as a normal distribution for analysis of variances could not be assumed, the indentation moduli distributions were tested with Kruskal-Wallis for equal medians. The test revealed a significant difference of median values ($p < 0.05$). To identify pairwise differences between multiple distributions Dunn's test was used as a post hoc with Bonferroni correction. It was determined that the median indentation modulus of collagen fibrils at development stage HH 38 differs significantly ($p < 0.05$) to the median value at HH41as is indicated in Figure 32. The median indentation moduli of single collagen fibrils from the developmental stages HH37 to HH41 respectively,

were found to be at 1.61 MPa, 1.63 MPa, 2.0 MPa, 1.63 MPa and 2.74 MPa. They differed significantly from 1.63 MPa at stage HH38 to 2.74 MPa at stage HH41.

In total, 7 to 20 collagen fibrils were indented at each development stage. Exact sample sizes for each development stage are listed in Table 3 and in the appendix. The table also gives an overview on the corresponding indentation moduli during embryonic development. The fibril numbers arise from the number of single collagen fibrils that could be imaged and identified at the chosen location as well as the original amount of collagen harvested from the different chick embryos. For HH41 a larger collagen sample mass was provided so that the representation shows the results of nanoindentation experiments on 48 individual fibrils at this stage.

Table 3: Median indentation moduli during embryonic development between HH37 and HH41 with corresponding p- values

HH Stage	# of Embryos	# of Fibrils	Indentation Modulus [MPa]	Q1 [MPa]	Q3 [MPa]	P-value
37	1	7	1.61	1.30	2.08	> 0.05
38	3	21	1.63	1.46	1.88	< 0.05 with HH41
39	1	9	2.00	1.62	2.25	> 0.05
40	1	17	1.63	0.98	3.52	> 0.05
41	3	48	2.74	1.50	3.64	< 0.05 with HH38

The results show a trend of a non-linear increase of the median indentation modulus during the progressing time of embryonic development. However, a significant difference could only be determined between stages HH38 and HH41. Also, the median indentation modulus at HH40 shows a lower value than expected at 1.63 MPa, considering the trend during development. At the early stages of development, the median indentation moduli show a lowest value of 1.61 MPa at HH37 and a highest median of 2.74 MPa at HH41. The nanoscale moduli at the early developmental stages from HH37 to HH39 additionally exhibit smaller interquartile ranges between 0.24 MPa to 0.78 MPa compared to later stages. Moduli at HH40 and HH41 show distinctly broader interquartile ranges at 2.54 MPa and 2.14 MPa, respectively. Although the increasing trend is more pronounced in the mean indentation moduli of the distributions during development from HH37 to HH41 and the corresponding standard deviations, they are not further discussed due to rejection of normality by the Shapiro-Wilk test.

5.1.2 Fibril Diameter in Air and PBS

Figure 33 shows the mean diameter of individual collagen fibrils at development stages HH37 to HH41. Statistical analysis with Shapiro-Wilk revealed normality of all distributions shown in the figure ($p > 0.05$). Levene's test showed the variances not to be significantly different ($p = 0.817$). Therefore, analysis of variances could be performed and revealed significant differences ($p < 0.01$) between the fibril diameter distributions. Significant differences of mean diameters in air could be determined via Tukey's pairwise post hoc test between HH39 and HH41 ($p < 0.05$) as well as HH40 and HH41 ($p < 0.05$). The fibril diameters measured in air, therefore show an increasing trend between HH39 and HH41.

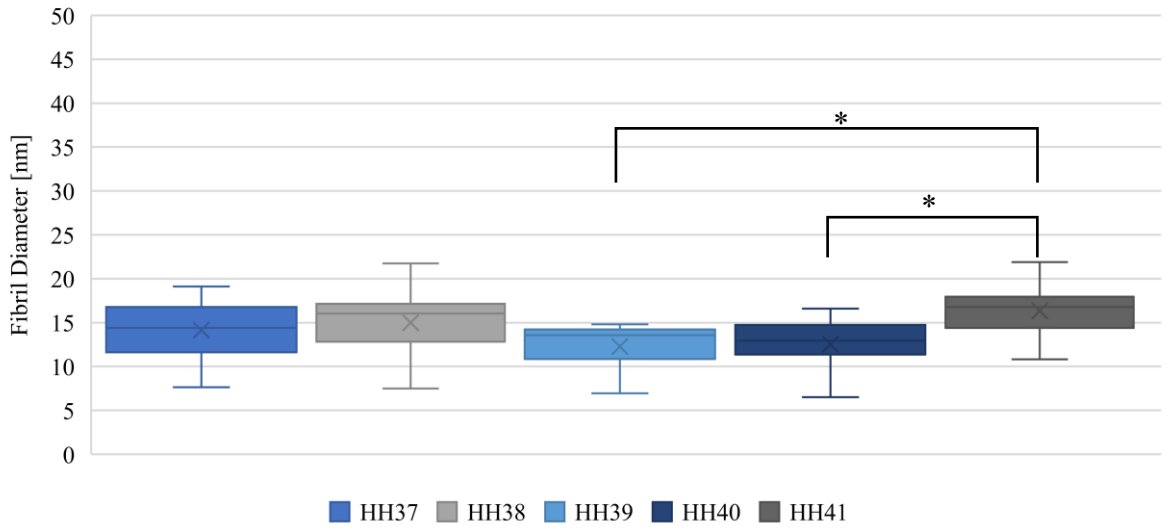

Figure 33: Fibril diameter in air at stages HH37 – HH41 shown as median (line), mean (x), interquartile ranges (boxes) and range (whiskers); Statistical indicator: * = $p < 0.05$

The smallest fibril diameter in air was found at 5.8 nm during stage HH38 while the largest diameter in air was recorded at 24.1 nm for stage HH41. The mean values of the fibril diameters in air at the stages HH37 to HH41 are 14.2 ± 3.4 nm, 15.0 ± 3.3 nm, 12.3 ± 2.6 nm, 12.5 ± 2.9 nm and 16.4 ± 3.2 nm, respectively. These values are also represented in Table 4.

After submerging the collagen fibrils in a PBS solution with a physiological pH value of 7.4 the mean fibril diameter of the collagen fibrils increased to the values shown in Figure 34. Again, statistical analysis was performed and showed the fibril diameters in PBS at all development stages to be normally distributed ($p > 0.1$). Levene's test showed the variances of populations to be significantly different ($p < 0.01$) so that the Welch t-test was performed to check for equal means. The test detected significant differences ($p < 0.01$) between the mean values. Pairwise testing revealed significant differences of fibril diameters in PBS between HH38 and HH39 ($p < 0.05$) as well as between HH39 and HH41 ($p < 0.05$). Similar to the

measured mean fibril diameters in air, the values show an increasing trend between HH39 and HH41. However, in contrast to the standard deviations measured in air, the diameters of hydrated fibrils show a clear increase of standard variations. This is especially noticeable at stage HH38 with a standard deviation of ± 3.3 nm in air and ± 8.3 nm in PBS. When compared to the values at HH37 and HH39 this development stage HH38 also shows a rather high mean value of the fibril diameters. The lowest and highest individual fibril diameter values in PBS were recorded during HH39 at 13.26 nm and during HH38 at 47.74 nm, respectively.

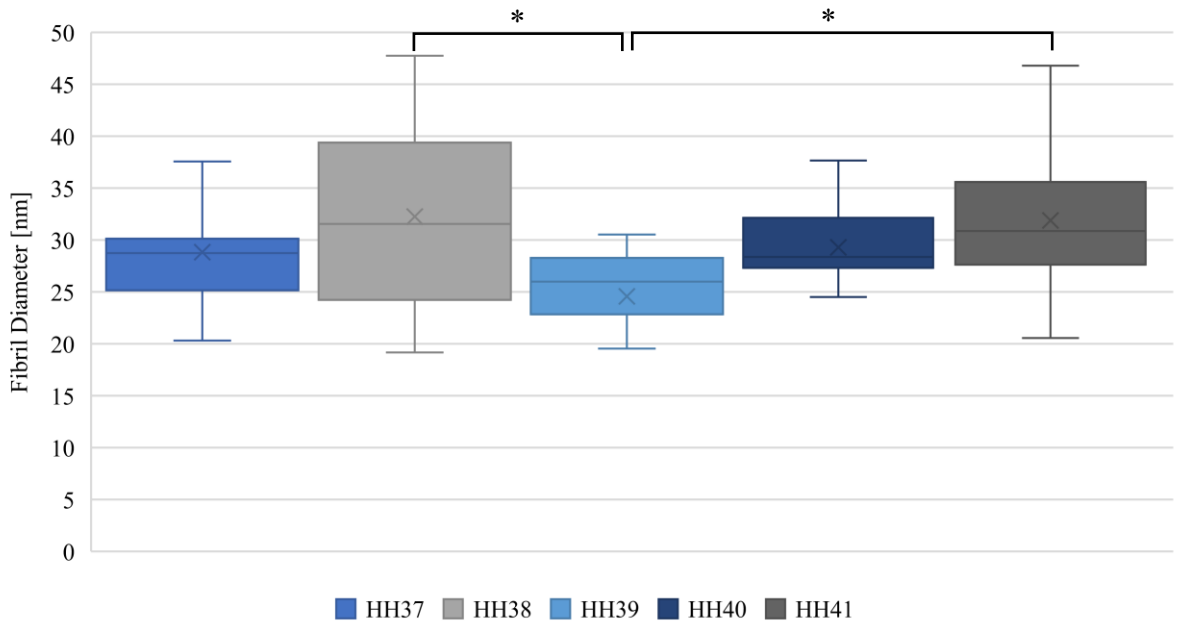

Figure 34: Fibril diameter in PBS at stages HH37 - HH41 shown as median (line), mean (x), interquartile ranges (boxes) and range (whiskers); Statistical indicator: * = $p < 0.05$

In PBS the mean fibril diameters were measured at 28.8 ± 5.5 nm, 32.3 ± 8.3 nm, 24.6 ± 5.4 nm, 29.3 ± 5.0 nm and 31.9 ± 6.1 nm for the continuing embryonic development stages from HH37 to HH41, respectively. The mean values are also presented in Table 4 for comparison. As the diameter increase of the hydrated fibrils in PBS seems to be proportional to the values recorded in air, the swelling ratios at the different developmental stages were calculated from the mean fibril diameter values in air and PBS (see Table 4). The results are illustrated in Figure 35.

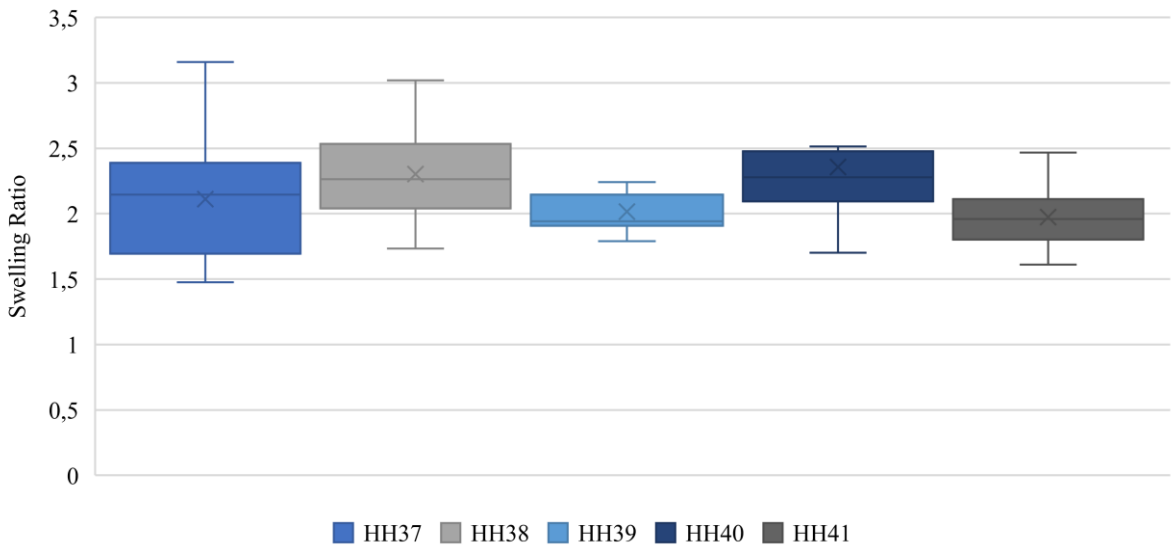

Figure 35: Swelling ratio of collagen fibrils at stages HH37 - HH41 shown as median (line), mean (x), interquartile ranges (boxes) and range (whiskers)

Statistical analysis showed the swelling ratio data sets to be normally distributed ($p > 0.05$) and equal in variances ($p = 0.27$). Analysis of variances revealed a slight significant difference of the distributions ($p = 0.049$). The plot correspondingly shows slight variations of the swelling ratios at the different development stages. However, they cannot be considered significant according to pairwise testing ($p > 0.1$). The lowest mean swelling ratio was calculated at HH39 and HH41 with 2.0 ± 0.3 while the highest mean swelling ratio lies at 2.4 ± 0.5 during stage HH40. The mean values of the swelling ratios commute around an overall mean swelling ratio of 2.1 ± 0.4. The results for the analysis of mean fibril diameters and swelling ratios are presented in the overview in Table 4 as mean ± standard deviation with corresponding p-values.

Table 4: Fibril diameters and swelling ratios during embryonic development, presented as mean ± SD with corresponding p-values

HH Stage	**37**	**38**	**39**	**40**	**41**
# of Embryos	1	3	1	1	3
# of Fibrils	18	21	9	17	48
Fibril Diameter in Air [nm]	14.2 ± 3.4	15.0 ± 3.3	12.3 ± 2.6	12.5 ± 2.9	16.4 ± 3.2
P-value	> 0.05	> 0.05	< 0.05 with HH41	< 0.05 with HH41	< 0.05 with HH39, HH40
Fibril Diameter in PBS [nm]	28.8 ± 5.5	32.3 ± 8.3	24.6 ± 5.4	29.3 ± 5.0	31.9 ± 6.1
P-value	> 0.05	< 0.05 with HH39	< 0.05 with HH38, HH41	> 0.05	< 0.05 with HH39
Swelling Ratio	2.1 ± 0.5	2.3 ± 0.4	2.0 ± 0.3	2.4 ± 0.5	2.0 ± 0.3
P-value	> 0.05	> 0.05	> 0.05	> 0.05	> 0.05

5.2 BAPN and Saline Treatment During Embryonic Development

5.2.1 Effect on Indentation Moduli

Prior to dissection of the chick embryos at stage HH40 two embryos were injected *in ovo* with 15 mg/g BAPN, while four others were injected *in ovo* with a saline solution. Figure 36 presents the results of nanoindentation experiments on the collagen samples harvested from these embryos. The representation shows the results of cantilever-based nanoindentation on approximately 22 collagen fibrils treated with BAPN and 76 collagen fibrils treated with saline.

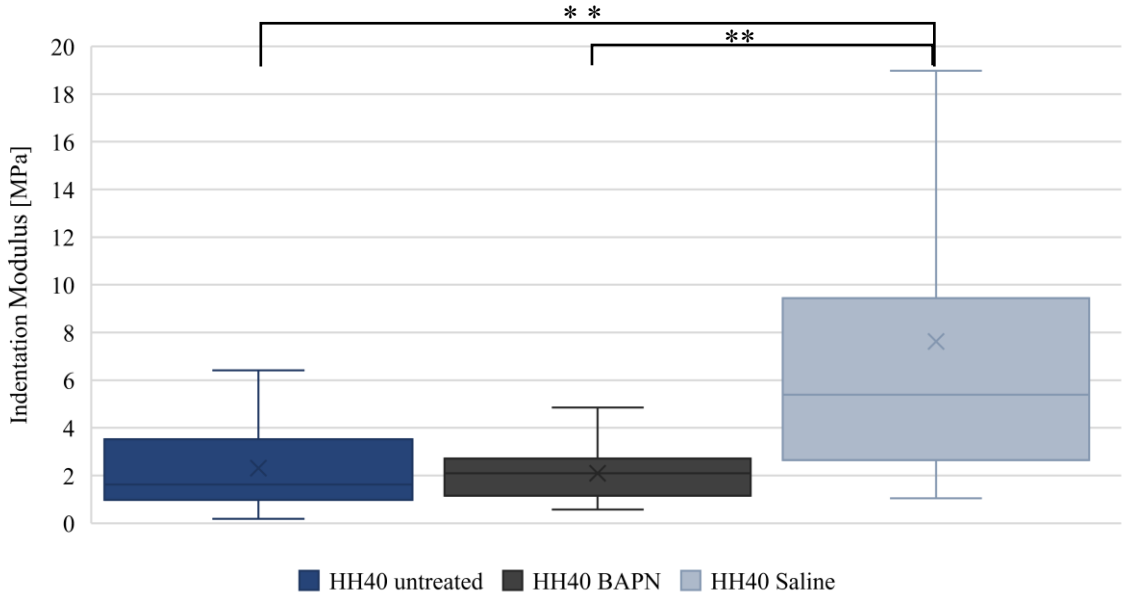

Figure 36: Indentation moduli collagen fibrils at HH40: untreated, treated with BAPN, treated with saline shown as median (line), mean (x), interquartile ranges (boxes) and range (whiskers); Statistical indicator: ** = $p < 0.01$

As was already established in the previous subchapter the data of indentation moduli at HH40 is not normally distributed ($p < 0.05$). Shapiro-Wilk testing also rejected normality of distribution for the indentation data set of collagen fibrils treated with saline ($p < 0.01$). The Kruskal-Wallis median test revealed significant differences between the sample group medians ($p < 0.001$). These could be determined via Dunn's pairwise post hoc test to be between the untreated sample group and saline treated samples ($p < 0.01$) as well as between BAPN and saline treated samples ($p < 0.01$).

The results show significant differences of the median indentation moduli between untreated samples at 1.63 MPa and samples treated with saline at 5.39 MPa. A significant difference could also be determined between the median indentation moduli of samples treated with BAPN at 2.1 MPa and the samples treated with saline. There is no apparent difference between untreated samples and samples treated with BAPN. However, the results of collagen fibrils treated *in ovo*

with saline show a larger interquartile range of 6.8 MPa compared to untreated samples and samples treated with BAPN. These exhibit interquartile ranges of 2.55 MPa and 1.62 MPa, respectively. An overview on the resulting values and the corresponding interquartile ranges as well as sample sizes and p-values is given in Table 5.

Table 5: Indentation moduli for collagen fibrils at HH40: untreated, treated with BAPN, treated with saline

Treatment	# of Embryos	# of Fibrils	Median Indentation Modulus [MPa]	Q1 [MPa]	Q3 [MPa]	P-value
Non	1	17	1.63	0.98	3.53	< 0.01 with Saline
BAPN	2	23	2.24	1.14	2.76	< 0.01 with Saline
Saline	4	76	5.39	2.64	9.44	< 0.01 with all

Due to considerable standard deviations of the results represented in Figure 36 another series of nanoindentation experiments was conducted with a different cantilever (type PNP-DB-20-B produced by Nano World). This cantilever possesses a lower force constant of 0.06 N/m when compared to the original cantilever model but the same resonance frequency of 17 kHz. It is therefore softer and even more susceptible to thermal drift and deflection, so that the nanoindentation experiments had to be carried out quickly and carefully. For these experiments 7 to 10 single collagen fibrils were indented per sample group as indicated in Table 6. The results of the nanoindentation experiments with this cantilever are shown in Figure 37.

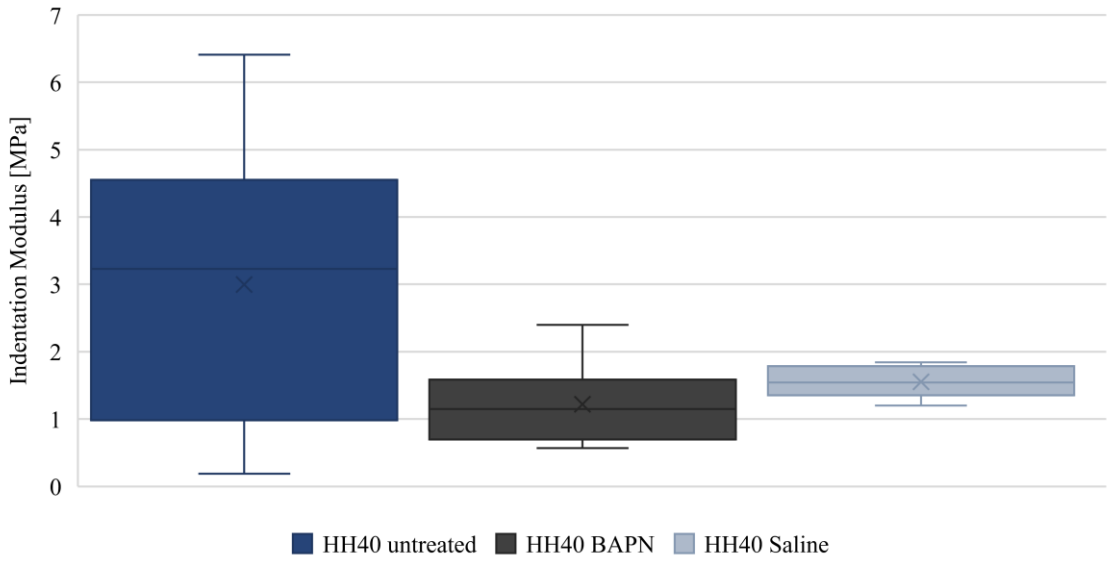

Figure 37: Indentation moduli of collagen fibrils at HH40 measured with cantilever PNP-DB-20-B: untreated, treated with BAPN, treated with saline; shown as median (line), mean (x), interquartile ranges (boxes) and range (whiskers)

The data distribution for all data sets was determined to be normally distributed by Shapiro-Wilk testing ($p > 0.1$). However, Levene's test showed the variances to be significantly different

($p < 0.01$). Therefore, Welch's t-test was performed on the data but showed no significant differences ($p = 0.12$) between sample means.

The indentation moduli calculated from these experiments for the samples treated with BAPN and saline show much smaller mean as well as median values than the resulting data of the previous, stiffer cantilever. On the other hand, the resulting values for untreated fibrils are distinctly higher than previously measured with the stiffer cantilever.

Table 6: Indentation moduli of collagen fibrils at HH40 treated *in ovo* with BAPN and saline with cantilever PNP-DB-20-B

Treatment	# of Embryos	# of Fibrils	Mean Indentation Modulus ± SD [MPa]	P-value	Median Indentation Modulus [MPa]	Q1 [MPa]	Q3 [MPa]
Non	1	7	3.0 ± 1.1	> 0.05	3.23	0.98	4.55
BAPN	1	9	1.2 ± 0.6	> 0.05	1.15	0.70	1.59
Saline	1	10	1.6 ± 0.2	> 0.05	1.55	1.36	1.79

For untreated collagen fibrils at HH40 measured with cantilever PNP-DB-20-B a mean indentation modulus at 3.0 ± 1.1 MPa was derived. The measurements with the softer cantilever on the sample treated with BAPN resulted in a mean indentation modulus of 1.2 ± 0.6 MPa and 1.6 ± 0.2 MPa for the sample treated with saline. The standard deviation for the treated sample groups, which can be derived from Table 6, was reduced considerably compared to experiments with the stiffer cantilever. However, no significant difference between the indentation moduli distributions recorded with the softer cantilever could be determined. Table 6 gives an overview on the recoded results via cantilever PNP-DB-20-B. The table includes median values and IQRs for easier comparison.

5.2.2 Effect on Fibril Diameter in Air and PBS

Figure 38 illustrates the results of the fibril diameter measurements in air and PBS for the treated and untreated samples at HH40. These measurements include the fibril diameters obtained by using the original cantilever type OPUS 4XC-NN and the softer cantilever type PNP-DB-20-B. The cantilever change had no impact on the height data recorded by the AFM.

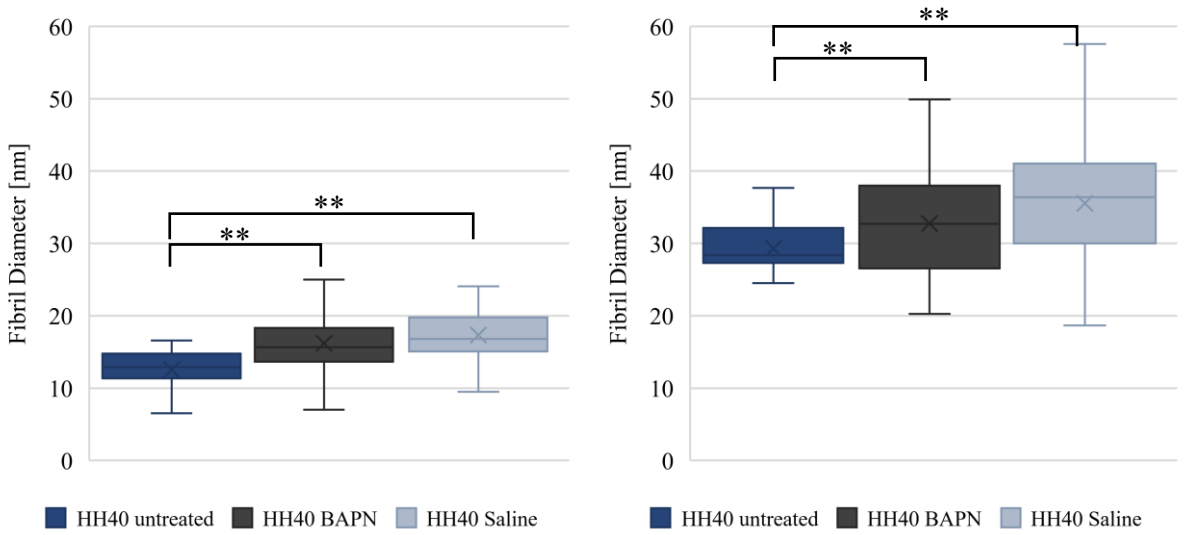

Figure 38: Fibril diameter at HH40 untreated and treated with BAPN and saline *left:* in air; *right:* in PBS; shown as median (line), mean (x), interquartile ranges (boxes) and range (whiskers); Statistical indicator: ** = $p < 0.01$

The fibril diameters in air and PBS were determined to be normally distributed via Shapiro-Wilk ($p > 0.05$). For diameters in air Levene's test showed no significant differences ($p = 0.9$) between variances. Analysis of variances revealed significant differences ($p < 0.001$) between the distributions of fibril diameter in air. A significant difference was found between the untreated fibrils and fibrils treated with BAPN ($p < 0.01$) and fibrils treated with saline ($p < 0.01$).

For diameters in PBS Levene's test showed no significant difference of variables ($p = 0.1$). Therefore, analysis of variances was performed and showed significant differences between the sample distributions ($p < 0.01$). Tukey's pairwise test showed significant differences in diameter between fibril diameters of saline treated samples and the other two sample groups ($p < 0.01$).

The mean fibril diameters show a small but significant difference in the samples treated with BAPN and saline in air as well as after hydration in PBS. The collagen fibrils treated with BAPN exhibit a mean fibril diameter of 16.2 ± 3.7 nm in air and 32.8 ± 7.7 nm in PBS. The collagen fibrils treated with saline on the other hand have a mean fibril diameter of 17.3 ± 3.0 nm in air and 35.6 ± 9.2 nm in PBS. The resulting swelling ratios for each of the three sample groups are represented in Figure 39.

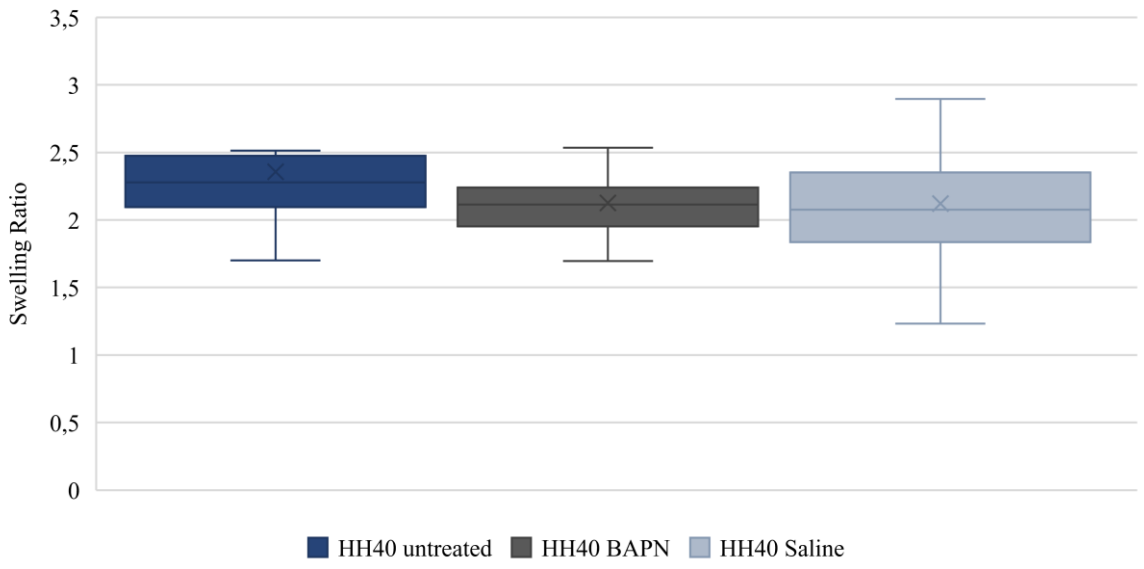

Figure 39: Swelling ratio of collagen fibrils at HH40 untreated and treated with BAPN and saline shown as median (line), mean (x), interquartile ranges (boxes) and range (whiskers)

Statistical evaluation showed the data to be normally distributed ($p > 0.05$) and equal of variances ($p = 0.06$). Analysis of variances revealed no significant differences between data distributions ($p = 0.99$). The mean fibril swelling ratio exhibits a no significant differences for either form of treatment compared to the untreated sample. The swelling ratios of the collagen fibrils treated with saline or BAPN also show no significant differences. For collagen fibrils treated with BAPN and saline, the mean swelling ratios were found to be at 2.1 ± 0.4 for both data sets. Therefore, they lie within the range of 2.1 ± 0.4 for all the other swelling ratios of collagen fibrils in PBS tested during this thesis. An overview on the fibril diameter and swelling values for the embryos treated with BAPN and saline is given in Table 7.

Table 7: Diameter values and swelling ratios for samples treated with BAPN and saline, presented as mean ± SD

Treatment	**Non**	**BAPN**	**Saline**
# of Embryos	1	2	4
# of Fibrils	17	35	82
Fibril Diameter in Air [nm]	12.5 ± 2.9	16.2 ± 3.7	17.3 ± 3.0
P-value	< 0.01 with Saline	< 0.01 with Saline	< 0.01 with Non, BAPN
Fibril Diameter in PBS [nm]	30.6 ± 7.2	32.8 ± 7.7	35.6 ± 9.2
P-value	< 0.01 with Saline	< 0.01 with Saline	< 0.01 with Non, BAPN
Swelling Ratio	2.4 ± 0.5	2.1 ± 0.4	2.1 ± 0.4
P-value	> 0.05	> 0.05	> 0.05

6 Discussion

6.1 Collagen Properties During Embryonic Development

The main goal of the research conducted during this thesis was to characterise the changes of biomechanical properties in individual tendon collagen fibrils during embryonic chick development. By using cantilever-based nanoindentation performed via AFM the indentation moduli of individual collagen fibrils were derived at different stages of embryonic development. The structural and mechanical properties of individual collagen fibrils were characterised throughout the range of embryonic chick development from HH37 to HH41. Force-indentation curves recorded by AFM indicated mechanical differences between the developmental stages. An increase of the indentation modulus during development was determined. However, while the resulting indentation moduli of embryonic collagen fibrils showed a nonlinearly increasing trend with continued development a significant difference ($p < 0.05$) could only be determined between HH38 and HH41. The analysed data on indentation moduli was not distributed normally at stages HH38, HH40 and HH41. Therefore, only median values of indentation moduli will be further discussed. The median indentation moduli of individual collagen fibrils were found to be changing significantly during embryonic development from 1.6 MPa at HH38 to 2.74 MPa at HH41. These findings correlate with previous investigations that discovered a significant increase of elastic moduli in developing tendon sections after HH38 [2], [7].

While cantilever-based nanoindentation is a promising tool for assessing individual collagen fibrils there are aspects of the process that can influence the results. During nanoindentation of collagen fibrils, the longitudinally aligned collagen molecules are compressed and bent by AFM tip apex but also by its sides as illustrated in Figure 40 [25], [27]. The shape of the cantilever imprint compares to an ellipsoid elongated along the longitudinal fibril axis due to the anisotropic material characteristics of collagen.

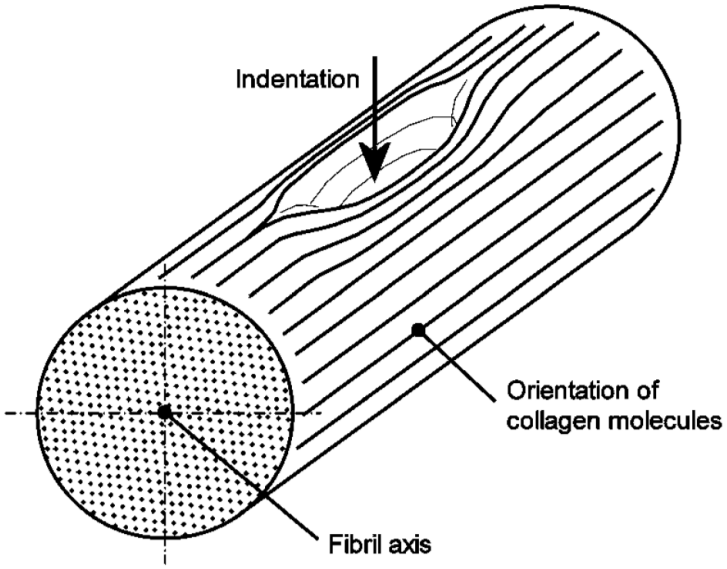

Figure 40: Artistic illustration of elliptical cantilever imprint on collagen fibril [27]

Indentation data is primarily recorded along the vertical axis of a fibril. When the AFM probe connects to the fibril surface the most dominant form of deformation is splitting of the collagen fibril into sub-fibrils. However, this deformation mechanism is preceded by initial stretching of the collagen triple helices on the lowest hierarchical level. Followed by sliding of collagen molecules relative to each other, molecular elongation and finally molecular slipping an applied force will results in the breakage of intramolecular cross-links [9]. Cross-links formed by covalent bonding between collagen molecules hold the fibril together and are one mechanism in connective tissues to increase the elastic modulus. Other mechanisms include extrafibrillar tissue components like GAGs that supposedly transmit interfibrillar loads due to their association with fibrillar surfaces, however several studies have provided information against this theory. Although tendon tissue mainly consists of collagen type I it also shows smaller amounts other collagens. Fibrillar collagens for example like collagens type III and V are known to form co-fibrils with collagen I [55], [56]. It has been speculated that fibril-associated collagens with interrupted triple-helices (collagens XII and XIV), which are another type of extrafibrillar proteins, are able to bridge collagen fibrils in tendon and contribute to tissue stiffness. However, due to removal of any proteoglycans during sample preparation, any influence of non-fibrillar structures on fibril mechanics was eliminated. Furthermore, the investigations of this thesis assessed individual collagen fibrils and their properties which, at this hierarchical level, are dependent on intrafibrillar interactions, i.e. cross-link formation.

From the results presented in the previous chapter (Tables 3-4 and Figures 32-35) it is apparent that in addition to the changes of median indentation moduli, the interquartile ranges of the moduli also seem to increase during embryonic development. The narrowest IQR was observed

during HH38 with 0.24 MPa while the broadest was found at HH40 with 2.54 MPa. In general, slight variations of the indentation moduli of fibrils within a development stage are expected and most likely primarily caused by individual differences of the fibrils. However, particularly large variations of the indentation moduli were detected at the late stages of embryonic development during HH40 and HH41. At HH41 this may be due to the larger number of fibrils and embryos (three, see Table 3) tested at this development stage. As for all biological materials inter-individual variations between individual donor organisms can have significant influences on material properties. This is also a likely explanation for the unexpectedly low median indentation modulus measured at stage HH40. Although the remaining embryonic stages show a non-linear increasing trend of indentation moduli the median value calculated for HH40 and the high IQR is an exception to this trend. Since only a single embryo was dissected at this stage for the investigations of this thesis, the low median value could be explained by individual aberrations of collagen fibril development in this donor embryo.

The mean fibril diameter of single collagen fibrils in air as well as hydrated in PBS was found to be significantly increasing ($p < 0.05$) between embryonic development stages HH39 and HH41. A significant difference was also detected for fibril diameters in air between HH40 and HH41 ($p < 0.05$) as well as for fibril diameters in PBS between HH38 and HH39. As all fibril diameter data was distributed normally mean values ± standard deviation are discussed. During embryonic development the mean diameter of collagen fibrils in air increases significantly from a value of 12.3 ± 2.6 nm at HH39 to 16.4 ± 3.2 nm at HH41. Proportionally, the diameter of hydrated collagen fibrils increases significantly from a value of 24.6 ± 5.4 nm at HH39 to 31.9 ± 6.1 nm at HH41. This trend of a broader collagen fibril diameter distribution with continued embryonic development has also been reported in previous studies by McBride et al. [38] and Fleischmajer et al. [57]. Since reference studies give a mean collagen fibril diameter value of up to 500 nm in mature chicken tendon measured via transmission electron microscopy [56], the increase of fibril diameter during embryonic development and maturation is apparent. Statistic evaluation of the recorded fibril diameter data during the experiments of this thesis shows a significant increase of fibril diameter only after development stage HH39 ($p < 0.05$), presumably due to the small sample size from HH37 to HH39 and the rather short development period investigated.

With increasing fibril diameter and indentation modulus, the indentation depth on the fibrils is reduced. A smaller indentation depth relates a higher contribution of surface tension to the indentation modulus. The surface roughness of collagen fibrils could have influenced the variation of the indentation moduli. All indentation data collected on the fibril apex was

recorded for an elongated pixel of the force map which slightly exceeded the scale of the D-banding and resulted in negligible roughness effects on the overall indentation moduli. This also makes possible variations of the indentation modulus negligible that arise from the overlap-gap arrangement of collagen molecules. As it has been suggested that due to density disparity the indentation modulus varies between the stiffer overlap and softer gap regions along a collagen fibril [26]. The surface roughness of a hydrated collagen fibril in PBS is illustrated in Figure 41 which presents the recorded height data in a sample force map.

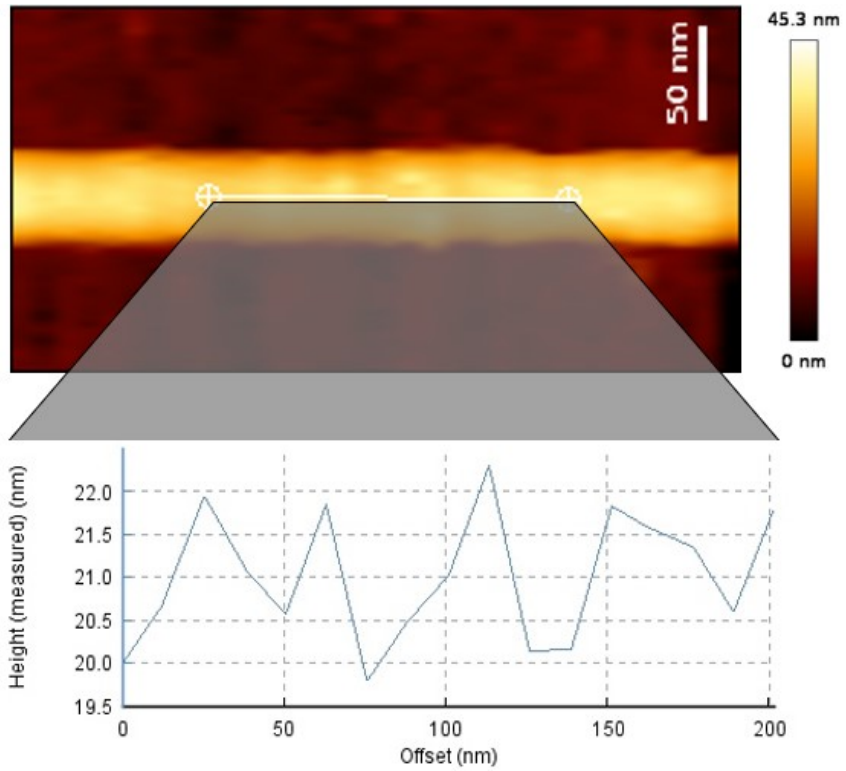

Figure 41: AFM height data on surface roughness of single collagen fibril (HH37) in PBS

The mean diameters of hydrated fibrils show standard deviations between 5.0 nm (HH40) and 8.3 nm (HH38). With increasing diameter variation in a sample group an effect of the glass substrate on the calculated indentation modulus is probable. With a maximum fibril diameter in PBS at 55.4 nm and a minimum diameter at 19.2 nm (at HH38) there are probable substrate effects on the fibrils with a lower diameter. Data on fibrils with such a small diameter of less than 20 nm in PBS was therefore not included in the presented results of indentation moduli. However, not all substrate affects could be barred from the results due to the small sample sizes at the earlier development stages. In this context all sample distributions were examined for correlation between fibril diameter in PBS and indentation modulus. The results of the statistical analysis are presented in the appendix. As can be seen in the sample distribution plotted in Figure 42 from HH 41 there is very little correlation between the fibril diameter and indentation

modulus which is not significant (r_s = 0.19, $p > 0.05$) so that substrate effects on individual fibrils cannot easily be identified from the distribution.

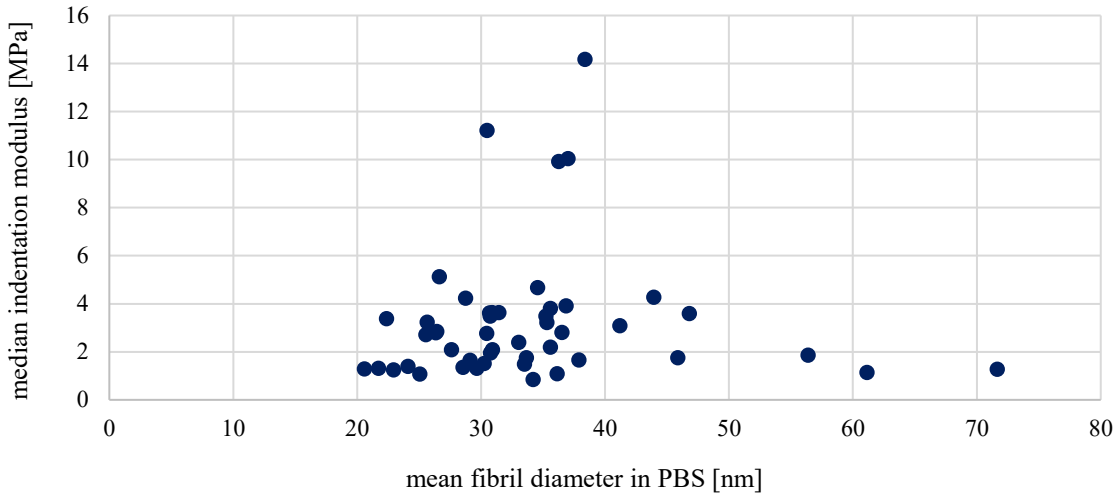

Figure 42: Distribution of calculated median indentation moduli at HH41

Nonetheless, following Buckle's rule, the optimal indentation depth on collagen fibrils to avoid the occurrence of any substrate effects is ideally at 6% of the fibril height, although indentation depths up to 15% can still be considered tolerable [25]. As the nanoindentation experiments in this thesis were all conducted with a predefined load of 0.5 nN, the indentation depths for the recorded data vary in respect to the individual fibril diameter. Indentation depth values taken from a random sample of force-indentation curves varied between 3 nm and 6 nm which indicates a substrate effect on part of the recorded data. This effect could not be visualized in any distributions of indentation moduli due to the small sample size at stages HH37 to HH40. A significant correlation (r_s = 0.87, $p < 0.01$) between increasing indentation moduli and hydrated fibril diameter distribution could be determined statistically at HH39. However, the coefficient shows a positive correlation and does therefore not indicate substrate effects which would be revealed as a negative correlation. No other sample distributions show any significant correlation between indentation moduli and fibril diameters.

Other factors that may have influenced the measured indentation moduli arise from the indentation procedure. For instance, lateral sliding of the AFM probe during small indentation depths could lead to discrepancies which alter the loading case and artificially increase the effective contact area between tip and sample. Also, the accuracy of the indentation modulus highly depends on the determination of contact area and contact stiffness (see chapter 4). For the experiments within this thesis the procedure for cantilever-based nanoindentation by Andriotis et al. [54] was employed. However, nanoindentation measurements on structures as

small as collagen fibrils with a mean diameter of 13.3 nm at HH39 in PBS are certainly pushing the limit of AFM capabilities. Therefore, the optimization of sensitivity calibration becomes necessary. During the experiments of this thesis it became important to optimize the calibration process of the inverse optical lever sensitivity. As can be derived from Figure 43 it is necessary to iterate the process at least once, sometimes more often, before setting the relative setpoint to the required value of 0.5 nN.

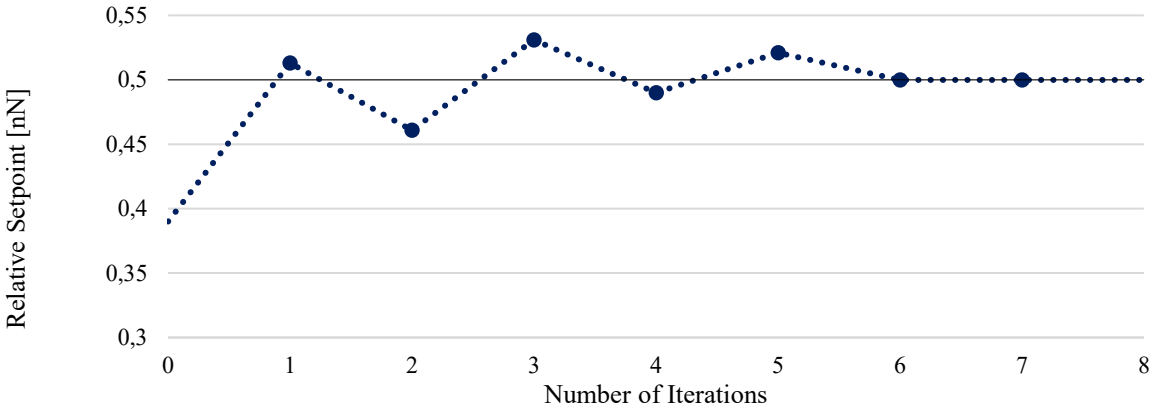

Figure 43: Optimization of inverse optical lever sensitivity calibration process

Otherwise, the true force applied to a collagen fibril during nanoindentation may deviate from the given setpoint value. It is also advisable to redo the optimized calibration process after every third force map recording as the optical lever sensitivity may change by slight thermal drift as well as lateral deflection. This is especially noticeable for soft cantilevers with low force constants like the cantilever model PNP-DB-20-B with a force constant of 0.06 N/m which was temporarily employed during this thesis.

The mechanical properties of developing embryonic tissues have been studied very little so far, presumably due to difficulty in handling fragile tissue constructs. Previous studies on embryonic tendon mainly focused on bulk tensile testing at late embryonic stages [38], [58], [59]. Most results compiled by those studies show very large differences. However, the increase of indentation modulus during the later stages of embryonic development found during the experiments of this thesis correlates with the reported behaviour of embryonic tendon properties in other works [2], [38]. While McBride et al. [38] reported an elastic modulus of 2.1 MPa at HH40 determined by bulk tensile testing of embryonic chick tendon, Marturano et al. [2] reported a significantly increasing nanoscale elastic modulus from 0.9 MPa to 1.3 MPa for embryonic chick tendon between HH38 and HH43, respectively. The findings of the study by Marturano et al. [2], presented on the left in Figure 44, were conducted on cryo-sectioned embryonic chick tendon with a nano- and microscale tip via FV-AFM. During embryonic

development from HH37 to HH41 they found the elastic modulus to be increasing from 0.9 MPa to 1.3 MPa using a sharp nanoscale tip (see Figure 44 left) and from 19 kPa to 21 kPa using a microscale tip with 5 µm radius. While the significant nonlinear increase of indentation modulus between 1.63 MPa at HH38 and 2.74 MPa at HH41 was also discovered for individual collagen fibrils during this thesis (see Figure 44 right), the median indentation moduli values varied.

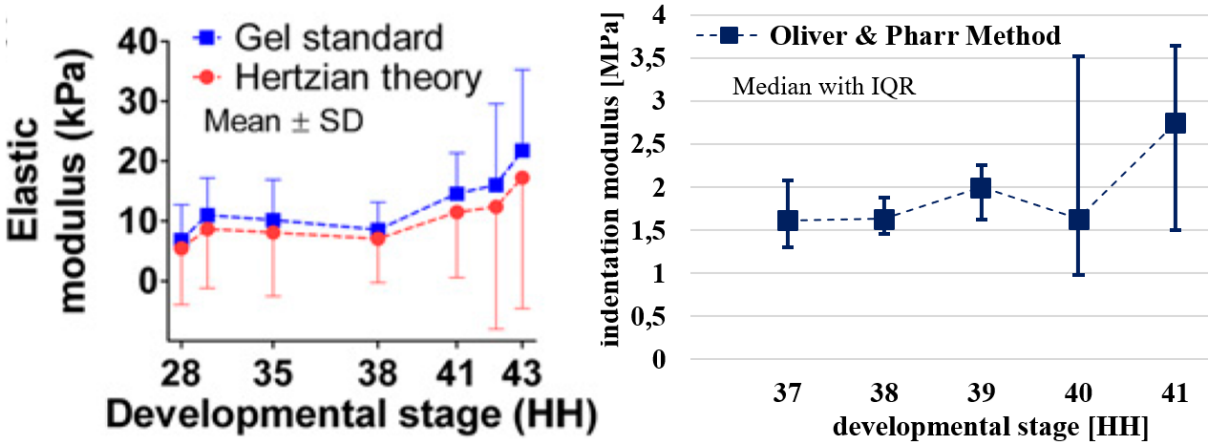

Figure 44: Indentation modulus during embryonic development *left:* mean nanoindentation results reported for tendon sections treated with saline *in ovo* [2]; *right:* median nanoindentation results on single collagen fibrils

However, Marturano et al. treated the chick embryos *in ovo* with saline and analysed the data gained through nanoindentation on tendon sections by using the Hertzian theory. When using the Hertzian theory for data analysis, the force-indentation data are fitted with equation 14. In equation 14 ν_{sample} is the Poisson's ratio, h the indentation, R_{eff} the effective radius and E_{sample} the indentation modulus which is the only fitting parameter [23].

$$F = \frac{3}{4}\frac{\sqrt{R_{eff}}}{\left(1-\nu_{sample}^2\right)}E_{sample}h^{3/2} \tag{14}$$

In case of cantilever-based nanoindentation the AFM tip may be assumed to be a sphere and the sample fibril a cylinder. This assumption can be used to estimate the effective radius using equation 15.

$$R_{eff} = \sqrt{\frac{R_{tip}^2 R_{fibril}}{R_{tip}+R_{fibril}}} \tag{15}$$

A study investigating the influence of analysis methods on the resulting indentation modulus showed the values calculated by Hertzian contact theory to be 34% percent smaller compared to the modulus calculated by using the Oliver Pharr method [23]. The analysis approach is therefore known to influence the resulting indentation modulus. Thus, direct comparison of the

resulting indentation moduli derived within this thesis to previous studies is not possible as the experiments differed profoundly in scale of tissue samples and methodology. Although some studies on the development of mechanical tendon properties during embryonic development were conducted before, none of them have focused on nanoindentation of individual collagen fibrils.

Overall the resulting nanoindentation moduli show a significant non-linear increase ($p < 0.05$) during embryonic development from a median value of 1.63 MPa at HH38 to 2.74 MPa at HH41 with an increasing IQR. Since extrafibrillar tissue components were removed during sample preparation, covalent cross-linking is the remaining known intrafibrillar mechanism to increase stiffness in collagen fibrils. Therefore, accumulation of cross-links during embryonic development may result in the observed difference of indentation modulus. This is also supported by the findings of a study that presented cross-linking density in tendon measured via multiphoton imaging as a marker of increased indentation modulus during tendon development [7]. A correlation between increasing elastic tendon modulus and hydroxylysyl pyridinoline-to-dry mass ratio in developing tendon was determined which indicates an increase due to cross-linking density.

6.2 LOX-Mediated Cross-Linking in Embryonic Collagen Fibrils

The effect of treating chick embryos *in ovo* with BAPN and saline was investigated during this study in regards to intrafibrillar cross-linking of collagen molecules as a potential mechanism of elaborating mechanical properties. Lysyl oxidases are a family of copper-dependent oxido-deaminases that modify the side-chain of lysyl residues in collagens. In adjacent collagen molecules the LOX enzyme thereby chemically separates lysine and hydroxy lysine residues to form aldehyde groups, which connect the collagen molecules through non-reducible inter-polypeptide chain cross-links [60]. This process of cross-linking enhances the mechanical properties of the tissue by stabilizing the fibrillar structure of collagen during self-assembly and preventing intermolecular slip [61]. BAPN is a LOX inhibitor and therefore prevents the formation of aldimine derived cross-links. It binds the active site of LOX which leaves the enzyme unable to assist in the formation of intrafibrillar cross-links between laterally aligned collagen molecules. In a previous study it was shown that inhibition of LOX activity via BAPN reduces mechanical properties in embryonic chick skin and bone [41]. It has also been found to

reduce the ratio of collagen to cross-link-indicating compounds [7]. LOX activity is therefore believed to influence the development of mechanical tendon properties significantly.

The nanoindentation data collected on collagen fibrils treated with BAPN and saline presented in the results (Tables 5-7, Figures 36-39) was recorded with two types of cantilevers that varied in force constants (0.3N/m for OPUS 4XC-NN and 0.06 N/m for PNP-DB-20-B). Although the calculated indentation moduli from both data sets are overlapping in their distribution, the indentation moduli determined with the stiffer cantilever OPUS 4XC-NN show larger interquartile ranges. This is founded mainly in the higher number of donor embryos and indented fibrils. However, high deviations of the mean fibril diameter in PBS also suggest substrate effects on smaller fibrils although that could not be determined by statistical evaluation of correlation ($p > 0.05$) between indentation modulus and fibril diameter. The resulting indentation moduli for fibrils treated *in ovo* with BAPN show no significant difference ($p = 0.74$) to the results of untreated collagen fibrils, however they do differ significantly from the samples treated with saline ($p < 0.01$). Discrepancies of the indentation modulus at HH40 from moduli at other developmental stages were already established in the previous subchapter and are likely due to individual aberrations of the single donor embryo. The untreated fibrils also show significantly lower ($p < 0.01$) indentation moduli than fibrils treated with saline. However, the significant increase of indentation modulus between saline and BAPN treated collagen fibrils indicates that BAPN does in fact inhibit the formation of enzymatic cross-links which results in a distinctly lower indentation modulus. On the other hand, already established cross-links do persist and remain untouched by LOX inhibition. The significant difference in indentation modulus due to BAPN treatment shows that LOX-mediated cross-links are an important factor contributing to fibril stiffness. Another possible factor that might contribute to fibril stiffness in a lesser extent is the formation of cross-links that are not LOX-mediated, e.g. transglutaminase mediated cross-links. Also, the non-enzymatic formation of isolated AGEs might be a possibility, although they are known to form with time during tendon maturation. A study on incubation of tendon with glucose to generate certain types of AGEs produced minimal mechanical effects [62]. Therefore, non-enzymatic cross-links are not thought to influence fibril stiffness during embryonic development significantly. However, some of these factors might contribute to the relatively high median indentation modulus of collagen fibrils at 2.24 MPa despite LOX inhibition. The data recorded with the softer cantilever PNP-DB-20-B in comparison, resulted in lower indentation moduli with lower standard deviation and IQRs for collagen fibrils treated with BAPN and saline. However, due to the small number of fibrils

indented for each sample group, statistical evaluation showed no significant difference of the populations ($p = 0.1$).

However, the data sets recorded with the cantilever OPUS 4XC-NN show a significant decrease ($p < 0.01$) of the median indentation modulus for the collagen fibrils treated with BAPN *in ovo* when compared to the samples treated with saline. The data showed a difference of 3.15 MPa in median indentation modulus due to BAPN treatment. This confirms that the repression of LOX via BAPN results in a significant decrease in the embryonic nanoscale modulus of tendon fibrils in response to the treatment. On the other hand, treatment *in ovo* with saline showed a significantly different ($p < 0.001$) median indentation modulus of 5.39 MPa at HH40 compared to all other untreated samples at different development stages. As saline does not have any known enzymatic effect it stands to reason that the increase in cross-linking may be due to a mechano-regulatory tissue response. It might be triggered by an increased ECM volume and pressure which was inflicted on the tissue by the saline injection 24 hours prior to dissection.

The study by Maturano et al. in 2013 [2] demonstrated that cross-linking modifies the mechanical resilience of collagen fibrils in respect to an unchanging bulk collagen content. They found a reduction in nanoindentation modulus of up to 38.8% on tendon sections at stage HH40 due to BAPN treatment *in ovo*. Although differing in scale of the sample material and analysis method this percentage correlates with the calculated percentage of reduction due to BAPN treatment of 41.6% in this thesis. Both values indicate the difference to samples treated with saline. Another study by Herchenhan et al. [60] that treated tendon fibroblasts *in vitro* with BAPN reported the formation of widely dispersed fibril diameters and irregularly shaped fibrils due to BAPN treatment. While the mean fibril diameters in PBS show larger variations and a significant diameter increase ($p < 0.01$) between BAPN and untreated samples, an also significant diameter increase ($p < 0.01$) was found between saline treated and untreated samples. Since no significant differences in diameter were recorded between BAPN and saline treated samples, the large fibril diameters might be due to a mechano-regulatory tissue response to the increased ECM volume. No irregular fibril shapes due to BAPN treatment were observed.

6.3 Collagen Fibril Hydration in PBS

The diameter of collagen fibrils increases when they are hydrated in PBS as water and ions are absorbed into the interstitial regions. The absorption of water is caused by the osmotically driven swelling of the fibrils. When a dry collagen fibril is placed in PBS the concentration of charged sites is higher within the fibril than in the PBS solution. Due to the chemical potential the charged collagen fibril extracts water and counter ions from the solution until an equilibrium is reached at the concentration gradient [63]. The hydration state of collagen fibrils factors into their mechanical response during indentation and can lead to differences in elastic moduli by two or three orders in magnitude. During loading the unbound water would partially be displaced and flow back into the fibril, following the concentration gradient, during unloading, which shows the poro-elastic behaviour of collagen fibrils. This change of elastic response arises from changes in the intermolecular interactions among neighbouring tropocollagens [26]. Therefore, it is important to characterise collagen fibrils while they are submerged in a solution with physiological pH to mimic the environment in which they perform their natural function within the body.

The investigations on the swelling of collagen fibrils during embryonic development showed no correlations between the swelling ratios of single collagen fibrils and their development stage ($p > 0.05$). The correlation coefficients are listed in the appendix. Furthermore, the inhibition of LOX activity via BAPN or treatment with saline *in ovo*, although causing a significant difference in fibril diameter ($p < 0.05$), had no significant effect on the fibril swelling ratio ($p = 0.55$). Statistical analysis resulted in no significant changes of the swelling ratios during embryonic development ($p > 0.1$). From all data sets an overall mean swelling ratio of 2.1 ± 0.4 for fibrils hydrated in PBS was calculated which corresponds to the findings of Grant et al. in 2009 [26] who reported an approximately two-fold swelling of mature bovine tendon collagen fibril diameters in a neutral buffer at pH 7.

The amount of water retained within the fibrils remains steady with regards to the collagen mass of the fibril. At an approximately twofold swelling of the fibril diameters there is more interstitial fluid than actual collagen substance. This becomes apparent when considering the volume increase of a collagen fibril. Assuming the collagen fibril as a perfect cylinder and that swelling of the collagen fibril in PBS only occurs radially and not axially ($l = l_{PBS} = l_{air}$), the fibril volume increases by a factor four (see Figure 45).

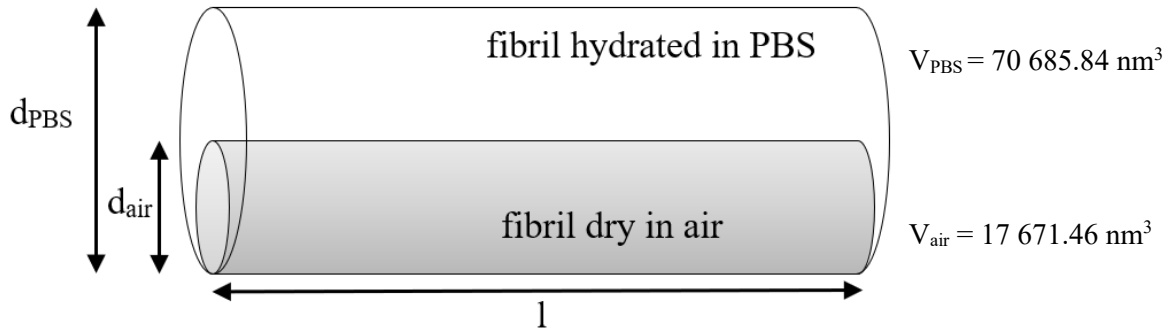

Figure 45: Artistic presentation of fibril volume increase due to hydration in PBS

This implies that the mass of a hydrated collagen fibril only covers one part of collagen and 3 parts of unbound water. The mass covered by water is even higher when adding the chemically bound water that remains within the fibril even during dehydration. The amount of water within the interstitial spaces in regards to the total fibril volume can be derived from equation 16.

$$\frac{V_{water}}{V_{collagen}} = \frac{V_{PBS} - V_{air}}{V_{air}} \tag{16}$$

A study by Avery and Bailey in 2008 [9] proposed that the increase in mechanical strength of collagen is achieved by cross-linking between fibres and fibrils which results in a tighter binding. They suggest that as a result of cross-linking the axial separation of collagen molecules is reduced which supposedly leads to a loss of unbound water within the collagen fibril. Although nanoindentation results of this thesis also suggest an increase in mechanical strength of individual collagen fibrils due to intrafibrillar cross-linking there is no apparent correlation between the increasing amount of cross-linking during development and fibril swelling ratios. While the indentation moduli of individual fibrils increase during embryonic development as a result of continued cross-linking between molecules within the fibril the swelling ratio shows no significant changes. Thus, no significant correlation ($p > 0.05$) between the increasing indentation modulus and fibril swelling ratio could be determined (see appendix for correlation coefficients). Even the inhibition of LOX mediated cross-linking via BAPN had no significant effect ($p > 0.05$) on the swelling ratio when compared to saline treatment which indicates that cross-linking between collagen molecules does not restrict swelling of the fibril.

6.4 Limitations and Further Investigation

Mechanical characterisation of individual collagen fibrils was conducted by implementing a procedure proposed by Andriotis et al. [54] for cantilever-based nanoindentation via AFM. Additionally, a protocol for the optimized calibration of the inverse optical lever sensitivity was developed to provide satisfactory results regarding accuracy and reproducibility while indenting collagen fibrils with small diameters. The AFM data was analysed by using the Oliver and Pharr method [53] which delivered accurate results. However, analysis methods used in other studies to interpret the data varied. Diverse methods exist and differ in assumptions, which leads to differences of the results and makes comparisons debatable. In the experiments of this thesis a substrate contribution was detected which influenced the resulting indentation moduli. The indentation experiments were conducted with an empirically determined relative setpoint of 0.5 nN. Due to the small fibril diameters derived from the AFM height data it might be beneficial to decrease the load even further to 0.3 nN. This would decrease the indentation depth on small fibrils and reduce substrate effects according to Buckle's rule. It would also be of interest to further investigate potential correlations between indention depth and modulus so that substrate effects are more apparent during analysis and can be avoided in future experiments. Nanoindentation performed with the cantilever model PNP-DB-20-B (force constant 0.06 N/m) resulted in decreased indentation moduli but was even more easily influenced by environmental changes and experiments were thus more time consuming although the recording time was reduced considerably. Therefore, a cantilever with a force constant of 0.3 N/m is advisable for further nanoindentation on embryonic collagen fibrils. Regarding continued investigations of embryonic collagen fibrils, a larger sample size of collagen fibrils and embryos between development stages HH37 and HH40 would be advantageous for a higher statistical significance level during evaluation. An interesting factor would also be the amount and location of enzymatic cross-links in embryonic collagen which could be determined additionally to nanoindentation. Immature cross-links can be determined by initially stabilizing the aldimine and keto-amine bonds by reduction with a mild reducing agent. This is followed by acid hydrolysis and subsequent separation from other amino acids by ion-exchange chromatography [9]. Any further studies characterising the properties of collagen during embryonic development may lead to a better understanding of natural tendon formation and help develop techniques to improve healing as well as regeneration of tendon.

7 Conclusion

The aim of this thesis was to investigate structural and mechanical properties of collagen fibrils during embryonic chick development. The investigations were conducted by cantilever-based nanoindentation according to the methodology and analysis approach proposed by Andriotis et al. [54]. By using this procedure and after successful calibration optimization of the inverse optical lever sensitivity, it was possible to assess collagen fibrils with diameters as low as 13.26 nm. Therefore, regarding cantilever-based nanoindentation, the AFM is a promising tool for nanomechanical assessment due to its broad range of environmental conditions and optimization potential.

During embryonic development the indented collagen fibrils exhibited a significant non-linear increase of median indentation moduli from 1.63 MPa at stage HH38 to 2.74 MPa at stage HH41. This indicates an accumulation of intrafibrillar cross-links between collagen molecules during embryonic development. Furthermore, a significant increase of the fibril diameter in air and PBS could be observed between HH39 and HH41 while the swelling ratios of the fibrils hydrated in PBS showed no significant changes. Therefore, in contrast to reports of previous studies no correlation between the amount of cross-linking and swelling ratio could be determined. Inhibition of enzymatic cross-linking *in ovo* with BAPN resulted in a significant decrease of indentation moduli of individual collagen fibrils compared to samples treated *in ovo* with saline. This concludes that emerging mechanical properties of tendon fibrils during embryonic development are in part due to LOX-mediated cross-linking.

The findings of this thesis contribute to expand the understanding of functional changes in tendon fibrils during normal embryonic development. This is an essential requirement to study abnormal aberrations that can occur during pathogenic formation or scarred healing of tendon. The ability to assess deviations from normal tendon formation in detail may enable pharmaceutical or tissue engineering strategies to intercept and redirect the tissue response. Functional properties of tissues are an essential component in assessment of tissue development in addition to typical gene, protein and morphological tissue markers.

Appendix

Table 8: Summary of sample sizes for experiments with cantilever model OPUS 4XC-NN

HH Stage	Indentation Measurements (Force-Maps)			Diameter Height Data	
	# of embryos	# of fibrils	# of force-indentation curves	# of embryos	# of fibrils
37	1	7	126	1	18
38	3	21	554	3	21
39	1	9	366	1	9
40	1	17	384	1	17
40 BAPN	2	23	485	2	35
40 Saline	4	76	2 581	4	82
41	3	48	1 519	3	48

Table 9: Summary of sample sizes for experiments with cantilever model PNP-DB-20-B

HH Stage	Indentation Measurements (Force-Maps)		
	# of embryos	# of fibrils	# of force-indentation curves
40 BAPN	1	7	86
40 Saline	1	9	114
41	1	10	165

Table 10: Correlation coefficients between increasing indentation moduli and fibril diameters in PBS during embryonic development

HH stage	Correlation coefficient r_s	P-value
37	-0.32	> 0.05
38	-0.05	> 0.05
39	0.87	< 0.01
40	0.47	> 0.05
40 BAPN	0.19	> 0.05
40 Saline	0.10	> 0.05
41	0.19	> 0.05

Table 11: Correlation coefficients between increasing indentation moduli and swelling ratios during embryonic development

HH stage	Correlation coefficient r_s	P-value
37	0.057	> 0.05
38	-0.27	> 0.05
39	0.50	> 0.05
40	0.43	> 0.05
40 BAPN	0.034	> 0.05
40 Saline	-0.13	> 0.05
41	-0.099	> 0.05

Figures

Tables

Bibliography

[1] E. A. G. Chernoff and D. A. Chernoff, "Atomic force microscope images of collagen fibers," *J. Vac. Sci. Technol. A Vacuum, Surfaces, Film.*, vol. 10, no. 4, 1991.

[2] J. E. Marturano, J. D. Arena, Z. A. Schiller, I. Georgakoudi, and C. K. Kuo, "Characterization of mechanical and biochemical properties of developing embryonic tendon," *Proc. Natl. Acad. Sci.*, vol. 110, no. 16, pp. 6370–6375, 2013.

[3] R. B. Svensson, T. Hassenkam, P. Hansen, M. Kjaer, P. Stig, R. B. Svensson, T. Hassenkam, P. Hansen, M. Kjaer, and S. P. Magnusson, "Tensile Force Transmission in Human Patellar Tendon Fascicles Is Not Mediated by Glycosaminoglycans Tensile Force Transmission in Human Patellar Tendon Fascicles Is Not Mediated by Glycosaminoglycans," vol. 8207, 2011.

[4] T. J. Lujan, C. J. Underwood, H. B. Henninger, B. M. Thompson, and J. A. Weiss, "Effect of Dermatan Sulfate Glycosaminoglycans on the Quasi-Static Material Properties of the Human Medial Collateral Ligament," vol. 11, no. July, pp. 894–903, 2007.

[5] S. E. Szczesny, K. L. Fetchko, G. R. Dodge, and D. M. Elliott, "Evidence That Interfibrillar Load Transfer in Tendon Is Supported by Small Diameter Fibrils and Not Extrafibrillar Tissue Components," no. October, pp. 2127–2134, 2017.

[6] N. R. Schiele, F. Von Flotow, Z. L. Tochka, L. A. Hockaday, J. E. Marturano, J. J. Thibodeau, and C. K. Kuo, "Actin cytoskeleton contributes to the elastic modulus of embryonic tendon during early development," *J. Orthop. Res.*, vol. 33, no. 6, pp. 874–881, 2015.

[7] J. E. Marturano, J. F. Xylas, G. V Sridharan, I. Georgakoudi, and C. K. Kuo, "Lysyl oxidase-mediated collagen crosslinks may be assessed as markers of functional properties of tendon tissue formation," *Acta Biomater.*, vol. 10, no. 3, pp. 1370–1379, 2014.

[8] C. Krotscheck, R. Wimmer, and M. Narodoslawsky, *Stoffliche Nutzung nachwachsender Rohstoffe in Österreich*. 1997.

[9] P. Fratzl, "Cellulose and collagen: from fibres to tissue," *Curr. Opin. Colloid Interface Sci.*, vol. 8, pp. 32–39, 2003.

[10] "No Title." [Online]. Available: https://image.slidesharecdn.com/collagendr-deb-110907120708-phpapp01/95/collagen-structure-distribution-synthesis-regulation-67-728.jpg?cb=1384942424.

[11] K. Gelse, E. Pöschl, and T. Aigner, "Collagens - Structure, function, and biosynthesis," *Adv. Drug Deliv. Rev.*, vol. 55, no. 12, pp. 1531–1546, 2003.

[12] J. Myllyharju and K. I. Kivirikko, "Collagens, modifying enzymes and their mutations in humans, flies and worms," *Trends Genet.*, vol. 20, no. 1, pp. 33–43, 2004.

[13] J. Khoshnoodi, J. P. Cartailler, K. Alvares, A. Veis, and B. G. Hudson, "Molecular recognition in the assembly of collagens: Terminal noncollagenous domains are key recognition modules in the formation of triple helical protomers," *J. Biol. Chem.*, vol. 281, no. 50, pp. 38117–38121, 2006.

[14] G. Ramachandran, *Biochemistry of Collagen*. Plenum Press, New York, 1976.

[15] Rockland Immunochemicals Inc., "No Title." [Online]. Available: http://rockland-inc.com/uploadedImages/ProductsStatic/15-01_Collagen_Figure2.png.

[16] D. F. Holmes, C. J. Gilpin, C. Baldock, U. Ziese, A. J. Koster, and K. E. Kadler, "Corneal collagen fibril structure in three dimensions: Structural insights into fibril assembly, mechanical properties, and tissue organization," *Proc. Natl. Acad. Sci.*, vol. 98, no. 13, pp. 7307–7312, 2001.

[17] Elsevier Inc., "No Title," *CellPress*, 2017. [Online]. Available: http://www.cell.com/cms/attachment/584373/4421946/gr2.jpg.

[18] E. Yamamoto, K. Hayashi, and N. Yamamoto, "Mechanical properties of collagen fascicles from stress-shielded patellar tendons in the rabbit," vol. 14, pp. 418–425, 1999.

[19] K. Hayashi, "Mechanical Properties of Collagen Fascicles From the Rabbit Patellar Tendon," vol. 121, no. February 1999, 2018.

[20] M. Jastrzebska and B. Barwinski, "Atomic force microscopy investigation of chemically stabilized pericardium tissue," vol. 388, pp. 381–388, 2005.

[21] J. Koivu, "Disulfide bonding as a determinant of the molecular composition of types I, II and III procollagen," *FEBS Lett.*, vol. 217, no. 2, pp. 216–220, 1987.

[22] B. Depalle, Z. Qin, S. J. Shefelbine, and M. J. Buehler, "Influence of cross-link structure, density and mechanical properties in the mesoscale deformation mechanisms of collagen fibrils," *J. Mech. Behav. Biomed. Mater.*, vol. 52, pp. 1–13, 2015.

[23] O. G. Andriotis, W. Manuyakorn, J. Zekonyte, O. L. Katsamenis, S. Fabri, P. H. Howarth, D. E. Davies, and P. J. Thurner, "Nanomechanical assessment of human and murine collagen fibrils via atomic force microscopy cantilever-based nanoindentation," *J. Mech. Behav. Biomed. Mater.*, vol. 39, pp. 9–26, 2014.

[24] R. B. Svensson, H. Mulder, V. Kovanen, and S. P. Magnusson, "Fracture mechanics of collagen fibrils: Influence of natural cross-links," *Biophys. J.*, vol. 104, no. 11, pp. 2476–2484, 2013.

[25] O. G. Andriotis, "Nanostructure and mechanics of collagen fribrils from osteogenesis imperfecta mice and chrinic asthma assessed with atomic force microscopy," 2013.

[26] C. A. Grant, D. J. Brockwell, S. E. Radford, and N. H. Thomson, "Tuning the elastic modulus of hydrated collagen fibrils," *Biophys. J.*, vol. 97, no. 11, pp. 2985–2992, 2009.

[27] M. P. E. Wenger, L. Bozec, M. A. Horton, and P. Mesquida, "Mechanical Properties of Collagen Fibrils," *Biophys. J.*, vol. 93, no. 4, pp. 1255–1263, 2007.

[28] Z. L. Shen, M. R. Dodge, H. Kahn, R. Ballarini, and S. J. Eppell, "Stress-Strain Experiments on Individual Collagen Fibrils," *Biophys. J.*, vol. 95, no. 8, pp. 3956–3963, 2008.

[29] The Fresh Healthcare Marketing, "ShoulderDoc," *ShoulderDoc*, 2017. [Online]. Available: https://www.shoulderdoc.co.uk/images/uploaded/tendon_stress_strain.jpg.

[30] V. Hamburger and H. Hamilton, "A series of normal stages in the development of the chick embryo," *J. Morphol.*, vol. 88, no. 1, pp. 49–92, 1951.

[31] Wordpress.com, "Bird Embryo," 2015. [Online]. Available:

https://geneflow.files.wordpress.com/2015/06/bird-embryo.jpg.

[32] R. A. Mccarthy and E. D. Hay, “Collagen I , laminin , and tenascin : ultrastructure and correlation with avian neural crest formation,” vol. 2, 1991.

[33] E. D. Hay, *Cell Biology of Extracellular Matrix*. Springer US, 1981.

[34] G. Kardon, “Muscle and tendon morphogenesis in the avian hind limb,” *Development*, vol. 125, no. 20, pp. 4019–4032, 1998.

[35] C. Kuo, B. Petersen, and R. Tuan, “Spatiotemporal protein distribution of TGFbetas, their receptors, and extracellular matrix molecules during embryonic tendon development,” *Dev Dyn*, vol. 237, no. 5, pp. 1477–1489, 2008.

[36] R. Schweitzer, “Analysis of the tendon cell fate using Scleraxis, a specific marker for tendons and ligaments,” *Development*, vol. 128, no. 19, pp. 3855–3866, 2001.

[37] D. Birk, M. Nurminskaya, and E. Zycband, “Collagen fibrillogenesis in situ: Fibril segments undergo post-depositional modifications resulting in linear and lateral growth during matrix development,” *Dev Dyn*, vol. 202, no. 3, pp. 229–243, 1995.

[38] D. McBride, R. Trelstad, and F. Silver, “Structural and mechanical assessment of developing chick tendon,” *Int. J. Biol. Macromol.*, vol. 10, no. 4, pp. 194–200, 1988.

[39] M. Kjaer, “Role of extracellular matrix in adaptation of tendon and skeletal muscle to mechanical loading,” *Physiol. Rev.*, vol. 84, no. 2, pp. 649–698, 2004.

[40] C. Couppé, “Mechanical properties and collagen cross-linking of the patellar tendon in old and young men,” *J. Appl. Physiol.*, vol. 107, no. 3, pp. 880–886, 2009.

[41] P. Fry, M. Harkness, R. Harkness, and M. Nightingale, “Mechanical properties of tissues of lathyritic animals,” *J. Physiol.*, vol. 164, pp. 77–89, 1962.

[42] G. Binning, C. Quate, and C. Gerber, “Invention of AFM,” *Phys. Rev. Lett.*, vol. 56, p. 930, 1986.

[43] W. H. Roos, “AFM 2-Dimensional Highresolution,” *Vrije Universiteit Amsterdam*, 2017. [Online]. Available: http://www.few.vu.nl/~wroos/AFM_2-Dimensional-HRes.jpg.

[44] JPK Instruments, *The NanoWizard AFM Handbook*. 2005.

[45] D. Johnson, N. Hilal, and W. R. Bowen, *Basic principles of atomic force microscopy*, no. December. Elsevier Ltd, 2009.

[46] D. Ricci and P. C. Braga, “Recognizing and Avoiding Artifacts in AFM Imaging,” *At. Force Microsc.*, vol. 242, pp. 25–38.

[47] D. Y. Abramovitch, S. B. Andersson, L. Y. Pao, and G. Schitter, “A tutorial on the mechanisms, dynamics and control of AFM,” *Proc.~American Control Conf.*, pp. 3488–3502, 2007.

[48] Burker Nano Surfaces, “Fundamentals of Contact Mode and TappingMode Atomic Force Microscopy,” *AZO Nano*, 2012.

[49] “ATOMIC FORCE MICROSCOPY - General Tutorial ATOMIC FORCE MICROSCOPY - General Tutorial,” *Microscope*, pp. 1–6.

[50] OPUS, “AFM Tip 4XC-NN,” *nano and more*, 2017. [Online]. Available: https://www.nanoandmore.com/AFM-Tip-4XC-NN.html.

[51] J. E. Sader, J. W. M. Chon, and P. Mulvaney, “Calibration of rectangular atomic force microscope cantilevers,” *Rev. Sci. Instrum.*, vol. 70, no. 10, pp. 3967–3969, 1999.

[52] J. Mamin, “TGT01,” *NT-MDT*, 2017. [Online]. Available: http://www.ntmdt-tips.com/products/view/tgt1.

[53] W. C. Oliver and G. M. Pharr, “Measurement of hardness and elastic modulus by instrumented indentation: Advances in understanding and refinements to methodology.,” *J. Mater. Res.*, vol. 19, pp. 3–20, 2004.

[54] O. G. Andriotis, S. W. Chang, M. Vanleene, P. H. Howarth, D. E. Davies, S. J. Shefelbine, M. J. Buehler, and P. J. Thurner, “Structure – mechanics relationships of collagen fibrils in the osteogenesis imperfecta mouse model,” 2015.

[55] D. E. Birk, “Type V collagen : heterotypic type I / V collagen interactions in the regulation of fibril assembly,” vol. 32, pp. 223–237, 2001.

[56] K. E. Kadler, D. F. Holmes, J. A. Trotter, and J. A. Chapman, “Collagen fibril formation,” *J. Biochem.*, vol. 316, no. Pt 1, pp. 1–11, 1996.

[57] R. Fleischmajer, B. R. Olsent, R. Timplt, J. S. Perlish, and O. Lovelace, “Collagen fibril formation during embryogenesis,” *Dev. Biol.*, vol. 80, no. June, pp. 3354–3358, 1983.

[58] H. L. Ansorge, S. Adams, D. Birk, and L. Soslowsky, “Mechanical , Compositional , and Structural Properties of the Post-natal Mouse Achilles Tendon,” *Ann Biomed Eng*, vol. 39, no. 7, pp. 1904–1913, 2011.

[59] N. S. Kalson, D. F. Holmes, A. Herchenhan, Y. Lu, T. Starborg, and K. E. Kadler, “Slow Stretching That Mimics Embryonic Growth Rate Stimulates Structural and Mechanical Development of Tendon-Like Tissue In Vitro,” no. October, pp. 2520–2528, 2011.

[60] A. Herchenhan, F. Uhlenbrock, P. Eliasson, M. Weis, D. Eyre, E. Karl, S. P. Magnusson, M. Kjaer, and E. Syndrome, “Lysyl Oxidase activity is required for ordered collagen fibrillogenesis by tendon cells 1,” 2015.

[61] S. Barenberg, F. Filisko, and P. Geil, “Ultrastructural deformation of collagen,” *Connect Tissue Res.*, vol. 6, no. 1, pp. 25–35, 1978.

[62] T. Andreassen, H. Oxlund, and C. Danielsen, “The influence of non-enzymatic glycosylation and formation of fluorescent reaction products on the mechanical properties of rat tail tendons,” *Connect Tissue Res.*, vol. 17, no. 1, pp. 1–9, 1988.

[63] S. Desissaire, “The effect of osmotic pressure on the mechanical and structural properties of individual collagen fibrils,” 2016.